Evaluating hydrodynamic parameters accounting for water retention hysteresis in a large sand column using surface GPR

Emmanuel Léger, Albane Saintenoy, Yves Coquet, Piotr Tucholka, Hermann Zeyen

Evaluating hydrodynamic parameters accounting for water retention hysteresis in a large sand column using surface GPR

Emmanuel Léger[1], Albane Saintenoy[2], Yves Coquet[3,4,5], Piotr Tucholka[2] and Hermann Zeyen[2]

Corresponding author: E. Léger, Lawrence Berkeley National Laboratory, 1 Cyclotron Road,Berkeley, CA 94720, USA. (eleger@lbl.gov)

[1]Lawrence Berkeley National Laboratory,
1 Cyclotron Road, Berkeley, CA 94720, USA

[2]GEOPS, Univ. Paris-Sud, CNRS,
Université Paris-Saclay, Rue du Belvédère,
Bât. 504, 91405 Orsay, France.

[3]Université d'Orléans, ISTO, UMR 7327,
45071, Orléans, France.

[4]CNRS/INSU, ISTO, UMR 7327, 45071,
Orléans, France.

[5]BRGM, ISTO, UMR 7327, BP 36009,
45060, Orléans, France.

Abstract. This study presents laboratory experiments using surface Ground Penetrating Radar measurements to monitor hysteresis of the water retention function of a sand. A GPR system monitored the volumetric water content changes in a large sand column submitted to different hydraulic heads applied at its bottom during one cycle of drainage followed by imbibition. The average velocity of the electromagnetic waves measured during drainage was consistently smaller than the one measured at the same applied head during imbibition. This was attributed to the hysteresis of the sand water retention curve. Coupled hydrodynamic and electromagnetic modeling was used to simulate radargrams whereas hydrodynamic modeling coupled with 1D optical ray path was used to estimate the hydrodynamic parameters of the sand from GPR reflection two-way travel times. Statistical and uncertainty analysis were performed on numerical and experimental data. The range of optimized parameters were compared to those obtained with classical laboratory methods such as the hanging water column and the constant head permeameter.

1. Introduction

Understanding water status and transport in the vadose zone requires accurate knowledge of the water retention function, $\theta(h)$, of the vadose zone materials as well as their hydraulic conductivity function, $K(\theta)$. The first one relates water pressure head, h, with volumetric water content, θ, while the later makes the link between hydraulic conductivity and volumetric water content or pressure head. This classical definition of the hydrodynamic functions assumes that h is a unique function of θ. However, as first pointed out by *Haines* [1930], this assumption is not valid because of hysteresis phenomena.

The basis of hysteresis theory, first observed in magnetism and adsorption on solids, was set in the works of *Néel* [1942, 1943], *Everett and Whitton* [1952]; *Everett* [1954, 1955] and *Preisach* [1935]. *Everett* [1955] and *Enderby* [1955] developed in parallel the independent domain theory, which was later suggested to be applicable to soil capillary hysteresis by *Collis-George* [1955]. The assumption behind the independent domain theory of soil-water hysteresis is that the pore space can be divided into discrete pores, each of which drains and fills independently of the state of other pores. The first published account of capillary hysteresis in term of independent domains was performed by *Poulovassilis* [1962], through experiments on glass bead materials. He observed hysteresis in the water retention function depending on wetting or drying processes and found good agreement between measurements and expected values from the independent domain theory. His results were pursued with success on sands by *Poulovassilis* [1970] and *Talsma* [1970]. However, disagreement between theory and experiments was also reported for glass bead material [*Topp and Miller*, 1966; *Morow and Harris*, 1965], for sand [*Vachaud and Thony*,

1971], for sandy loam [*Topp*, 1969] and for silty loam and clay loam [*Topp*, 1971]. These studies suggest that the independent domain theory applies only to data obtained during static-equilibrium or steady state flow conditions but fails to depict hysteresis properly in case of unsteady flow [*Topp*, 1971].

Following Topp's conclusion, *Mualem* [1973] improved and developed a new formalism based on the similarity hypothesis [*Philip*, 1964]. This hypothesis is based on the assumption that the pore water distribution function can be described as a product of two independent functions, the pore opening radii distribution and the pore body radii distribution. This new formalism resulted in a succession of papers [*Mualem*, 1973, 1974; *Mualem and Dagan*, 1975; *Mualem*, 1977] where Mualem's formalism of hysteresis is improved. These works gave the basis of the currently known Mualem's theory of hysteresis, finally developed and published in *Mualem* [1984].

In parallel to the models presented above, qualified as conceptual, empirical models have been proposed based on fitting water retention curves data. They are defined for specific types of soils and do not claim general validity because their derivation is not based on a physical representation of hysteresis. In the present study, we will use the empirical model of *Kool and Parker* [1987], based on the scanning model of *Scott et al.* [1983], applied to sand.

Knowledge of the water physical state in soil is required for understanding hydrostatic and hydrodynamic processes in soils. Methods exist for sampling directly the vadose zone, but they can disrupt the system of interest and can rarely, if ever, provide the sampling rate (spatial or temporal) required to fully understand the complex, interrelated processes that operate in this zone.

A large amount of classical laboratory methods have been developed to obtain the hydraulic properties of soil samples. Depending on soil type and/or the parameters aimed to be retrieved different techniques were designed such as, the hanging water column [*Dane and Hopmans*, 2002], the evaporation methods [*Wind*, 1966; *Peters and Durner*, 2008], or the multi-step outflow [*Eching and Hopmans*, 1993; *Eching et al.*, 1994]. The hanging water column method can get the soil-water retention function parameters for the drainage and wetting phase whereas the multi-step outflow experiment allows to obtain the hydraulic conductivity parameters as well as the soil-water retention function parameters. These classical methods are robust and already proved their efficiency. However they need quite a long experimental time (several days), are facility-demanding and can not be run *in situ* on the field.

Advances in electronics in the past thirty years have significantly reduced the costs and improved the acquisition rates of geophysical methods. Their non-invasive nature makes them highly suitable for studying the vadose zone. Among them, electrical resistivity [*Zhou et al.*, 2001; *Goyal et al.*, 2006] and electromagnetic [*Sheets and Hendrickx*, 1995; *Akbar et al.*, 2005] measurements such as Nuclear Magnetic Resonance (NMR) [*Knight et al.*, 2012] and Ground Penetrating Radar (GPR) [*Huisman et al.*, 2003] are the most commonly used. They provide physical properties, such as electrical conductivity, NMR relaxation time constants and dielectric permittivity. These parameters are highly sensitive to soil composition, structure, density and water content.

The field of hydrogeophysics is developing since decades [*Vereecken et al.*, 2008; *Lesmes and Friedman*, 2005; *Huisman et al.*, 2003; *Hubbard and Rubin*, 2000]. However, few

studies dealt with geophysical measurements as data to be fitted to quantify the hysteresis of water retention and hydraulic conductivity functions.

Knight [1991] conducted laboratory resistivity measurements on sandstone samples during imbibition and drainage. She found that the resistivity measured during imbibition was consistently less than the one measured at the same saturation during drainage. She attributed this difference to the presence of electrical conduction at the air/water interface and concluded on the dependence of the geophysical properties on saturation history. This first study on the effect of pore-scale fluid distribution on the electrical behavior during imbibition and drainage was followed by several others [*Knight and Abad*, 1995; *Fleury and Longeron*, 1998; *Moss et al.*, 1999].

Lai et al. [2006] gave a GPR evidence of hysteresis of soil water functions. They acquired GPR measurements over soil and asphalt at various degrees of saturation. Their data exhibited dielectric hysteresis for both soil and asphalt, depending on drying or wetting processes.

More recently *Weihnacht and Boerner* [2014] performed a GPR monitoring of the soil water content in a high rectangular Plexiglas® tank filled with homogeneous sand. They used transmission radar data, one antenna on each side of the tank, at different depths to obtain the volumetric water content during a moving water table experiment. The obtained data showed different sand water retention functions for drainage and imbibition. Despite the fact that no hydrodynamic modeling was used, the idea of coupling GPR measurements with Multi-Step Outflow (MSO) experiment was already an advancement.

The Institute of Environmental Physics in Heidelberg University recently performed interesting studies [*Dagenbach et al.*, 2013] and [*Klenk et al.*, 2015]. They used the ASSES-

GPR test site to monitor the water table during fluctuating water table experiments. Both studies were inspired by the precursory works of *Tsolfias et al.* [2001] and *Endres et al.* [2000] interested in capillary fringe observation with GPR. *Dagenbach et al.* [2013] set a stationary GPR antenna installed at the soil surface and recorded a trace at constant time step. They studied the experimental capillary fringe reflections during drainage and imbibition and compared them to those obtained numerically with three different water retention models, namely *Brooks and Corey* [1964] and the constrained and unconstrained *van Genuchten* [1980] models. The study they conducted on the capillary fringe reflection, amplitude and phase is similar to the one carried by out *Saintenoy and Hopmans* [2011] and *Diamanti and Redman* [2014]. *Klenk et al.* [2015] performed radargram profiles at different experimental times and studied the wavelet associated with peculiar reflections during drainage/relaxation/imbibition cycles. Their comparison between numerical modeling and experiments allowed them to obtain information on the relative hydraulic properties of the materials.

All the studies presented above did not go further than qualitative measurements and paved the way for hydrodynamic parameter estimation using geophysical methods and particularly GPR.

In the present study we developed an inversion method to obtain the Mualem-van Genuchten (M-vG) [*Mualem*, 1976; *van Genuchten*, 1980] parameters characterizing separately the drainage and the imbibition water retention curves. To achieve this goal, we first set up numerical experiments to test the possibility of characterizing hysteresis from GPR data acquired with commercial antennae placed at the top of a soil column subjected to controlled water table variations. We provided an inversion of the synthetic data to

obtain the M-vG parameters characterizing independently water retention functions for drainage and imbibition.

The aim of the study was to develop a method able to obtain parameters as accurate as the classical laboratory methods but with a much shorter experimental time. This goal has been realized by working under dynamical conditions.

Uncertainty analysis was conducted using multiple inversions performed on independent noise-added synthetic data. Finally we inverted experimental GPR data acquired in a laboratory experiment to retrieve hydraulic properties in drainage or wetting condition of a large sand column. The dispersion observed in the data, namely shift in frequency, is taken into account to model the observed phenomena. Statistical analysis on the experimental data is drawn using bootstrapping method [*Efron*, 1979]. The results are compared with the M-vG parameters estimated from classical laboratory experiments such as hanging water column [*Dane and Hopmans*, 2002] and falling head experiments.

2. Background

2.1. Soil hydraulic functions

The soil hydraulic functions can be described by several mathematical expressions [*Kosugi et al.*, 2002] requiring a different number of parameters depending on the chosen model. For the $\theta(h)$ relationship, one of the largest groups of models represented in the literature is the power function model of the form:

$$(1 - S_e^{-a})^b S_e = \alpha h, \tag{1}$$

where $S_e = \frac{\theta - \theta_r}{\theta_s - \theta_r}$ is the effective saturation, θ_s is the saturated volumetric water content, θ_r the residual volumetric water content, and α (>0), a and b, are fitting parameters.

Many models based on this power form have been proposed to fit water retention data, such as those presented in *Gardner* [1958], *Brooks and Corey* [1964], *Fredlung and Xing* [1994] and *van Genuchten* [1980] among others. Their mathematical equivalence was studied by *Fuentes et al.* [1992].

In the current study we used the equation from *van Genuchten* [1980],

$$S_e = (1 + (\alpha h)^n)^{-m}, \tag{2}$$

where α is the inverse of the absolute value of the soil matric potential at the inflection point of the $\theta(h)$ curve. The two dimensionless fitting parameters, n and m, are linked by

$$m = 1 - \frac{k}{n}, \tag{3}$$

with $n > k$ [*Haverkamp et al.*, 2005; *Leij et al.*, 2005]. For simplicity, k takes integer values which correspond to different models giving closed form analytic expressions for the hydraulic conductivity functions. The case $k = 1$ corresponds to the model of *Mualem* [1976], while $k = 2$ gives the conductivity model of *Burdine* [1953]. Using $k = 1$, the hydraulic conductivity function is written as

$$K(\theta) = K_s S_e^{\lambda} \left[1 - \left[1 - S_e^{\frac{n}{n-1}}\right]^{\frac{n-1}{n}}\right]^2, \tag{4}$$

with K_s the saturated hydraulic conductivity and λ a parameter accounting for pore tortuosity. The whole description of water flow in the unsaturated zone, considering no hysteresis, with equations (2) and (4) requires the determination of 6 parameters: θ_r, θ_s, n, α, K_s and λ.

The choice of *van Genuchten* [1980]'s model for describing the water retention function was motivated by the good fitting of our hanging water column data and by hydrodynamic modeling reasons since *van Genuchten* [1980]'s model was the only one taking into

account hysteresis in the Hydrus1D code that we used for hydrodynamical modeling (see section 2.5).

2.2. Hysteresis of the water retention function

A schematic representation of hysteresis for the soil water retention curve is presented in Figure 1. The boundary hysteresis loop consists of the main drying (red) and main wetting (green) curves, following the model of *van Genuchten* [1980]. In our study, we will use this model because it is implemented in the Hydrus1D code to solve the hydrodynamical equations with hysteresis. In this theoretical representation, the main drying curve is described by the van Genuchten parameter vector, $vG^d = \{\theta_r^d, \theta_s^d, n^d, \alpha^d\}$. The main wetting curve is described by $vG^w = \{\theta_r^w, \theta_s^w, n^w, \alpha^w\}$. Considering only the hysteresis on the water retention function, we are left with a total of eight unknown parameters to determine.

On the basis of the work of *Šimunek et al.* [1999] and *Likos et al.* [2013], we will assume

$$\theta_r^w = \theta_r^d = \theta_r, \tag{5}$$

$$\theta_s^w = \theta_s^d = \theta_s, \tag{6}$$

and

$$n^w = n^d = n. \tag{7}$$

The two first conditions imply that changes in the volume of entrapped air during rewetting due to temperature differences are disregarded [*Hopmans and Dane*, 1986]. The last condition imposes that the curvature of the two water retention functions are similar. We will see later in section 4.1, that this last assumption is representing well the hysteresis cycle measured for the Fontainebleau sand used in our experimental data. Imposing these

constraints has the advantage of further reducing the number of model parameters, but will obviously result in some loss of flexibility in describing the hysteresis of the water retention function, since the main drying and main wetting curves differ only by their α values.

2.3. Electromagnetic wave velocity as a function of soil dielectric properties

Surface GPR consists of two antennae, being electric dipoles, positioned on the surface of the medium to be sounded. The transmitting antenna emits short pulses of spherical electromagnetic (EM) waves in response to an excitation current source. The receiving antenna converts the incoming EM fields to electrical signals. Following the work of *Annan* [1999], the velocity of an electromagnetic wave propagating in a non-magnetic soil, with low electrical conductivity, is

$$v = \frac{c}{\sqrt{\varepsilon'}}, \tag{8}$$

where ε' denotes the real part of the relative dielectric permittivity and c denotes the velocity of EM waves in air (0.3 m/ns).

2.4. Petrophysical Relationships

A petrophysical relationship linking dielectric permittivity to water content is needed to interpret GPR measurements. The bulk soil has a frequency-dependent relative dielectric permittivity ε_b, expressed by a complex number with the loss factor represented by the imaginary part, defined as:

$$\varepsilon_b = \varepsilon_b^{'}(f) - i\left[\varepsilon_b^{''}(f) + \frac{\sigma_b}{2\pi f \varepsilon_0}\right], \tag{9}$$

where f is the frequency, $\varepsilon_b^{'}(f)$ the real part of soil permittivity, $\varepsilon_b^{''}(f)$ the imaginary part, including the relaxation loss, and σ_b the bulk conductivity leading to conductivity

losses. ε_0 is the permittivity of free space. In the literature, petrophysical models are divided into four categories: effective-medium, empirical, semi-empirical and volumetric models [*Alharthi and Lange*, 1987; *Knoll*, 1996; *Shivola*, 1999]. We used the volumetric CRIM model [*Birchak et al.*, 1974; *Roth et al.*, 1990], where the relative dielectric permittivity of the porous geological material, ε_b, is a function of the material porosity, its state of saturation and the respective permittivity of each of its individual constituents. The soil we used in our experiments was a Fontainebleau sand. Using the CRIM relationship for a tri-phasic medium composed of water, air and silica, we obtain

$$\varepsilon_b^\gamma = \theta\varepsilon_w^\gamma + (1-\phi)\varepsilon_s^\gamma + (\phi-\theta)\varepsilon_a^\gamma, \tag{10}$$

where ε_w, ε_s and ε_a are respectively the dielectric permittivity of water, silica and air, ϕ the porosity and θ the volumetric water content. γ is an empirical coefficient that depends on soil structure, set to 0.5 in this study. The dielectric permittivity of air is real and its value is set to be the same as in vacuum, thus its relative permittivity is equal to 1. We measured $\varepsilon_s = 2.23$ using a time-domain reflectometer. We assumed that the solid phase was non conductive and therefore its dielectric permittivity was independent of frequency. The permittivity of water ε_w is a function of frequency and conductivity, and is expressed in time domain by Debye's equation [*Debye*, 1929]:

$$\varepsilon_w = \varepsilon_\infty + \frac{\varepsilon_{st} - \varepsilon_\infty}{1 + i\omega\tau}, \tag{11}$$

in which $\varepsilon_\infty = 4.9$ is the high-frequency limit of the real dielectric permittivity, $\varepsilon_{st} = 80.088$ the static value of the real dielectric permittivity at 20°C [*Klein and Swift*, 1977], τ is the relaxation time of water at 20°C [*Stogryn*, 1971]. We further assumed that there was no loss due to the bound water, or at least it was negligible for the soil used.

2.5. Hydrodynamical Modeling

In this study we considered one-dimensional vertical soil water flow described by the one-dimensional *Richards* [1931]'s equation expressed in terms of water content as

$$\frac{\partial \theta}{\partial t} = \frac{\partial K(\theta)}{\partial z} + \frac{\partial}{\partial z}\left[K(\theta)\frac{dh}{d\theta}\frac{\partial \theta}{\partial z}\right], \tag{12}$$

where $K(\theta)$, and $\theta(h)$ are described by the Mualem-van Genuchten model, presented in equations (2) and (4).

We used the Hydrus-1D code [*Šimunek et al.*, 2008] to solve this equation, with an atmospheric (Neumann) boundary condition at the top. We changed the bottom boundary conditions with time (through a Dirichlet boundary condition) using the evolution of the applied hydraulic head we used in our experiments. The considered media was divided into 5 mm thick horizontal layers, thin compared to the shortest wavelength of the electromagnetic waves propagating through it.

2.6. Electromagnetic Modeling

2.6.1. Finite Difference Time Domain

Numerous techniques are available for simulating GPR data, such as ray-based methods (e.g. *Cai and McMechan* [1995] or *Sethian and Popovici* [1999]), time-domain finite-difference full-waveform methods (e.g. *Kunz and Luebbers* [1993] or *Kowalsky et al.* [2001]), or the Finite Differences Time Domain (FDTD) method (e.g. *Irving and Knight* [2006]). We used the GprMax2D code [*Giannopoulos*, 2005], which uses FDTD modeling to solve Maxwell's equations in 2 dimensions. The synthetic radargrams presented below have been simulated using GprMax2D.

2.6.2. 1D velocity modeling

To avoid time-consuming FDTD modeling in our inversion algorithm, we computed the Two Way Travel Time (TWT) of the wave reflected at the bottom of the tank assuming a 1D propagation through a stack of 5 mm thick layers. The electromagnetic wave inside each layer was computed with equation (8) taking the dielectric permittivity value defined by equations (10) and (11), and the water content distribution modeled by HYDRUS-1D. We took into account the dispersion of the wave due to the Debye relaxation phenomena, evaluated for the maximum frequency of the considered reflection. To do so, we selected a time window where the bottom tank reflection wavelet was included and took the dominant frequency resulting from Instantaneous Fast Fourier Transform (IFFT). However, this observed dispersion originated from two phenomena, Debye dispersion and variations of the antenna coupling through time. These two phenomena are difficult to separate in experimental data. However, we show that this dispersion was included in the TWT uncertainties in the numerical simulations showed in the next section.

3. Numerical experiments

3.1. Set-up

We considered a homogeneous cylindrical medium (71 cm height and 60 cm diameter), with a porosity set to 0.39 and hydrodynamic properties in the range of what we measured with water hanging column experiments and UMS Ksat System on Fontainebleau sand (section 4.1). These parameters are summarized as p_{in} in Table 1. A transmitter (emitting a Ricker wavelet centered on 1000 MHz) and a receiver were positioned at the sand column surface. The draft of the apparatus is presented in Figure 2. The tube on the right indicates the different water table levels set during the experiment. The two triangles symbolize the GPR transmitter and receiver. A very thin layer of Perfect Electrical

Conductor (PEC) was positioned at the bottom of the sand column. At the initial state, the water level was set at the top of the column, corresponding to $h_0 = 71$ cm.

Different hydraulic heads were applied to the bottom of the cylinder. The hydraulic heads were chosen in agreement with experimental data, in order to later compare numerical radargrams with experimental ones.

Two types of experiment were conducted: i) a multi-step (subscript MS) experiment where we applied successively $h_1 = 41.5$ cm, $h_2 = 31.5$ cm, $h_3 = 22.5$ cm, $h_4 = 0$ cm, $h_5 = h_3$, $h_6 = h_2$, $h_7 = h_1$ and $h_8 = h_0$ at experimental times $t_{MS} = [100; 1600; 2700; 4000; 5800; 6900; 7900; 9200; 10500]$ seconds, and ii) a one-step (subscript OS) experiment where the heads applied to the bottom of the cylindrical medium were $h_0 = 71$ cm, $h_1 = 0$ cm and $h_2 = h_0$ at experimental times $t_{OS} = [700; 6600; 8100]$.

A volumetric water content profile was computed at each experimental time step using Hydrus-1D with the M-vG parameters p_{in} presented in Table 1. The hysteresis effect was fully represented by the parameter α, taking $\alpha_w = 2\alpha_d$ according to *Kool and Parker* [1987] and *Šimunek et al.* [1999]. The two water retention functions (wetting and drying curves) corresponding to the parameters p_{in} are shown on Figure 1. Arrows symbolize the direction of the cycle, first drainage then wetting. The GPR antenna set at the top was used to monitor the water content of the sand, using the TWT of the reflection on the PEC surface at the bottom of the tank.

3.2. Forward modeling

3.2.1. 1D velocity modeling

The water content profiles generated at each experimental time step were converted to permittivity profiles using relations (10). The TWT of the PEC reflection was computed

using the 1D velocity modeling. Figure 3 displays the TWTs obtained when varying the water table levels with the multi-step protocol (a), and the one-step protocol (b).

In both cases, we present the TWTs obtained from the simulated water content profile accounting for hysteresis of the water retention function following the model of *Kool and Parker* [1987] (red circles) and without hysteresis (blue curves). As expected, since the simulated water content profiles during the drying and wetting cycle will be different for the same heads applied, the TWTs will be consequently different. The major advantage of our experiments resides in making measurements during dynamical processes, without waiting for hydrostatic equilibrium. We see that the TWTs are different from the TWTs obtained while the sand is wetting (Figure 3-a) for $h = 31.5$ and 22.5 cm). Working under non-equilibrium allows to decrease the whole experimental time.

3.2.2. Finite Difference Time Domain

The water content distribution outputs from Hydrus-1D were used as inputs for the GprMax2D code using equations (10) and (11). The simulated GPR monitoring of the dynamic water level variation is presented in Figure 4-a) for the multi-step and 4-b) for the one-step case. The reflection on the PEC layer at the base of the sand is arriving between 15 and 22 ns. Because of relaxation losses due to the presence of water, and the dielectric permittivity gradient due to retention properties of the medium the electromagnetic wave is traveling through, the frequency spectrum of the electromagnetic wave changes while it is propagating. The dominant frequency associated with the bottom tank reflection found between 15 and 22 ns will thus evolve with the applied head. This is represented in Figure 5, where the maximum of the instantaneous frequency associated with this reflection is presented for each experimental time step. On this figure, we display the

picking of the maximum instantaneous frequency as circles and the TWT of the bottom tank reflection picked from the radargrams presented in Figure 4 (red line). The drier the column, the higher the frequency content is, and, similarly, the wetter the column, the more present are the relaxation effects, the steeper is the dielectric permittivity gradient, and the smaller is the frequency content of the bottom tank reflection.

3.3. Uncertainty analysis

3.3.1. Data uncertainty quantification

As stated above, the frequency shift observed in the numerical radargrams (Figures 4 and Figure 5) has two sources: Debye relaxation and the permittivity gradient created by the retention properties of the medium. Our 1D-velocity modeling does not take into account these sources of signal dispersion and we observe a small discrepancy between the picking of the reflection presented in the radargram 4-a) and b) and our 1D velocity algorithm results. These two TWT curves are displayed on Figure 6-a) for the one-step protocol. The Root Mean Squared Error (RMSE) between these two curves is 0.09 ns.

An other source of uncertainty in our data is the one associated with the applied head. For determining the TWT uncertainties associated with the applied hydraulic head uncertainties, we considered the RMSE between the TWT curve resulting from the hydraulic head presented in section 3.1 for the one-step experiment, and one other TWT curve generated with the initial hydraulic head h_0 decreased by 1 cm. These TWT curves are presented in Figure 6-b), where the red curve represents TWT computed with initial hydraulic head, whereas blue curve represents the initial hydraulic head -1 cm. The RMSE between these curves is 0.11 ns. At last we considered the picking uncertainties by considering that time picking can not be better than the one time step, which was 0.058

ns for experiments presented in section 4.3. Even if the time-step was much smaller for the numerical experiment we chose to take the experimental time step in order to better represent the uncertainty. Taking these three sources of uncertainties in our one-step numerical experiments, we estimated our overall uncertainty associated with each TWT data point, using a quadratic summation, to $\sigma_{OS} = 0.15$ ns. The uncertainties for the multi-step case was computed with the same procedure to $\sigma_{MS} = 0.13$ ns.

3.4. Inversions on Numerical Data Perturbed by Gaussian Noise

We used the TWT of the bottom tank reflection as presented in Figure 3-a) for the multi-step experiment and 3-b) for the one-step case as data to be fitted to get the set of M-vG parameter values $\boldsymbol{p} = \{\theta_r, \theta_s, \alpha_d, \alpha_w, n, K_s, \lambda\}$. The optimization procedure was the Shuffled Complex Evolution (SCE-UA) algorithm [*Duan et al.*, 1992] minimizing the objective function expressed as the RMSE between the modeled and observed TWT of the bottom tank reflection to be fitted. This RMSE was given by

$$RMSE = \sqrt{\frac{1}{N}\sum_{j=1}^{N}[\tau_{xp}(t_j) - \tau_{mod}(t_j, \boldsymbol{p})]^2}, \tag{13}$$

where τ_{xp} is the radargram-measured TWT generated with the hydrodynamic parameters $\boldsymbol{p_{in}}$ at experimental time t_j, and τ_{mod} is the modeled TWT reflection at time t_j subject to soil hydraulic parameter vector $\boldsymbol{p}$, and N is the number of points used for comparisons, i.e. the number of considered experimental times t_j.

We sampled the parameters in ranges defined according to the values found in the literature. The range for θ_r was $[0.01; 0.1]\, cm^3/cm^3$, the one for θ_s was $[0.3; 0.4]\, cm^3/cm^3$. K_s interval was $[0.05; 3]\, cm.min^{-1}$, n was allowed to get values between 2 and 10, and α_W and α_d ranges were both set to $[0.01; 0.1]\, cm^{-1}$. We set the λ range to $[0; 10]$, considering

this parameter as a fitting one. The historical paper of *Mualem* [1976] proposed λ values in the range of $[-1; 2.5]$ and conclude on a good fitting for most soils with $\lambda = 0.5$. This value is the most used in the literature. The studies of *Schaap and Leij* [2000]; *Schaap et al.* [2001]; *Schaap and van Genuchten* [2005] were among the first to develop wider range for λ parameter $[-1; 1]$. We then based our λ range on the study of *Wösten et al.* [1999], on the database of European soils, where λ could reach values higher than unity.

For each generated parameter set $\boldsymbol{p}$, we computed the TWT of the bottom tank reflection using the 1D velocity model. This inversion modeling procedure is presented as a flow diagram in Figure 7, where the objective function is the RMSE. We used 20 complexes, 50,000 iterations for each loop and a constraint on 30,000 iterations to stop if no better model was found during the Complex search.

Since the inversion algorithm, SCE-UA, is not following the Bayesian rule, the statistical analysis performed on one single inversion cannot be considered as mathematically correct (see the works of *Vrugt et al.* [2003] for discussion on this topic). We decided to perform a statistical analysis on models obtained by independent SCE-UA optimization procedures carried out on different noise-added generated TWT data. Examples of the perturbed TWT are presented in Figure 8 as purple points. These data correspond to the original simulated one, in blue, to which we added small time delays sampled from a Gaussian distribution centered on the original value, with standard deviation $\sigma_{MS} = 0.13\ ns$ for the multi-step case and $\sigma_{OS} = 0.15\ ns$ for the one-step case.

We performed 80 inversions on 80 different Gaussian noise-added data in both cases. In the multi-step case, we selected the models with associated RMSE smaller than or equal to 2 $\sigma_{MS} = 0.26\ ns$. In the one-step case, we selected the models with associated

RMSE smaller than or equal to 2 $\sigma_{OS} = 0.30\ ns$. Possible double models were taken out in order to keep the same weight for all models, and not influence the histograms. It resulted on 968,291 models in the multi-step case and 448,507 models in the one-step case. The statistical distributions of each parameter of all the selected models are presented in Figure 9-a) for the multi-step case and Figure 9-b) for the one-step case. The value for each parameter set as input is represented with the vertical dashed orange bar and can be found in Table 1.

Except for θ_s and λ these histograms show that the input parameters are included in every distribution. The volumetric water content at saturation is over estimated by a mean value of 0.025 % in both experimental procedures.

The histograms presented in the one-step case, on Figure 9-b) seems to have more difficulty than the multi-step case, to estimate accurately the parameters α_d, and α_w. One possible reason for α_w is the rewetting phase observed with only 10 data points in the one-step case, and 40 points in the multi-step case (compare Figure 3-a) and b)). In addition, inter-correlation between parameters exist, as presented in Figure 10, where objective function plots are displayed for the multi-step case (a)-c)-e)-g)) and one-step case (b)-d)-f)-g)). The objective function plots are different depending on the experimental case (multi or one-step). This means that the inter-correlation observed is partially due to the theoretical link between parameters as well as the design of the experiment.

One can see on 10-a)-b)-c)-d) correlations between K_s and α_w and n. Figures10-g)-h) show a link between λ and n depending on the experimental protocol. These objective function plots show that the regions with lowest RMSE (dark blue areas) always con-

397 tain the input parameter, except for *lambda*. This is particularly well illustrated on the
398 Figure 10-e) where we see that $\alpha_w = 2\alpha_d$ corresponds to the dark blue region.

399 The case of λ parameter and its link with parameters require another analysis. On
400 Figures 8-a) we displayed 3 TWT curves of the bottom tank reflection for the one-step
401 case. The set of parameters taken for the original blue line data is the one set as input
402 (Table 1). The two other lines represent the result of an increase or a decrease of the n
403 value by 2. Increasing n results in increasing the TWT variations and vice-versa. Figure 8-
404 b) shows as well the effect of an increase or a decrease of the parameter λ. At the opposite
405 of n, increasing λ from 0.5 to 2 results in decreasing the TWT variations. Figures 8-c)
406 and d) are the equivalent for the multi-step case. From these figures, we see that different
407 couples of (n, λ) will fit as well the noisy data (purple points). A too small n value
408 associated with a too small λ value will result in the same curve than too high values for
409 both n and λ. This is illustrated by the objective function plot Figure 10-g).

410 In addition, multi-step data are not sensitive to λ variations in the first three steps and
411 the last one (Figure 8-d)), whereas most of the one-step data are sensitive to this parameter
412 variations. This might explain differences in the two experimental data inversion results.

413 This numerical analysis showed the robustness of our modeling for inverting most of
414 the hydrodynamic parameters as well as some difficulties due to inter-correlations between
415 parameters. However, we see that working under dynamical processes, without waiting for
416 static equilibrium at each step, did not prevent us to retrieve most of the hydrodynamical
417 parameters even if we applied a quite brutal uncertainty analysis. For instance, we applied
418 the same uncertainty to every point of the TWT data not considering the influence of the
419 frequency shift uncertainties is stronger when the soil is becoming drier. In addition, an

uncertainty of 1 cm on the hydraulic head is a pessimistic estimation. To be convinced that the noise we added was really strong, Table 1 shows the optimized parameters retrieved on non-noisy data with a RMSE smaller than 0.015 ns.

4. Laboratory Measurements

4.1. Characteristics of the sand

The van Genuchten water retention parameters were obtained by fitting the data obtained with three hanging water column (HWC) experiments performed on Fontainebleau sand core (250 cm^3) samples packed at 1.67 $g.cm^{-3}$ bulk density. We considered uncertainties on h at $\sigma_h = 1\ cm$, $\theta = 0.03\ cm^3.cm^{-3}$. We suspect that some evaporation happened, which gave the low value on θ_r parameter. The van Genuchten parameters obtained are presented in Table 2, under the label "Lab. meas.".

Figure 11 shows the retention curves data acquired from the HWC experiments. They were fitted using the van Genuchten model. As expected for this type of soil, α_w was close to $2\alpha_d$. The HWC results confirmed that the n parameter could be considered as independent from drying or wetting processes, since the curvature of the water retention curves are very similar for drying and wetting branches.

The saturated hydraulic conductivity was determined on several 250 cm^3 soil core samples packed at 1.6 g/cm^3, using the UMS Ksat System, under constant head. The range of values obtained are presented in Table 2. The λ parameter was not determined, but its value was initially expected to be close to 0.5 [*Mualem*, 1976] without having any other measurements.

Granulometric determinations on the Fontainebleau sand used for the experiments showed that 13% of its grains had a diameter larger than 0.25 mm and 98% larger than

0.125 mm. Its average particle density was 2.8 ± 0.1 g cm^{-3}. The sand was packed to a porosity estimated to be 0.39.

4.2. Experimental Set-up

The experimental apparatus consisted of two cylindrical tanks (80 cm height and 60 cm diameter), one tank, T_S, filled with the Fontainebleau sand and the other one, T_w, filled with water at a level corresponding to the hydraulic head. T_s was filled with 321 kg of sand, compacted manually in order to obtain a bulk density of $\rho_b = 1.7\ g.cm^{-3}$. The sand layer was put on top of a 5 cm gravel layer in order to drain and wet homogeneously the sand. To obtain a strong reflection at the bottom of the sand we put between the gravel layer and the sand a thin aluminum sheet, finely meshed, to let the water go through. Three pictures of the experimental set-up are presented in Figure 12. Figure 12-a) shows T_w, where we see the holes used as overflow to maintain the water table during drainage and where we see the green water supply pipe. T_s and T_w bottoms were linked through four independent plastic tubes with taps (Figure 12-b)). Figure 12-c) displays T_s with the antenna set at the top of the sand, maintained in position by a load. The white thin layer is a geo-textile enclosing the sand. Piezometers were connected at the bottom of each tank to indicate the applied head.

4.3. Experimental measurements

Four experiments were carried out using this experimental setup. For each experiment, the whole soil profile was initially water saturated in order to be on the main drainage curve during the first cycle. Both tanks were hydraulically separated by closing the taps on the linking tubes. The level of water was set to the desired level (for example 42

cm) in T_w using an overflow hole. Then the hydraulic contact between both tanks was established again, opening the taps. The water drained out of T_s was evacuated through the overflow hole in T_w. This procedure was repeated for all steps during draining and wetting processes.

The radargram measured during one of the multi-step experiment is shown in Figure 13-a), and during a one-step experiment, in Figure 14-a). The horizontal axis is the experimental time in seconds, and the vertical axis is the TWT in nanoseconds. During the drainage and imbibition cycle, the direct wave signal evolves through time, due to the evolution of the media properties surrounding the antennae, which affects the antennae coupling. The reflection on the aluminum sheet at the base of the sand is arriving around 28 ns, other reflections are tank side effects. As expected the TWT of this reflection evolves with the water table level. In the multi-step experiment, the heads were changed at [800;1500;2000;2900] seconds for drainage and [4400;5200;5800;6800] seconds for re-wetting. On Figure 13-b, we display the instantaneous maximum frequency of the considered reflection. On this figure we display as well the TWT of this reflection, relative to its initial TWT, when saturated. We see that the behavior of this reflection is comparable to the one we simulated (Figures 3, 4 and 5). Despite the fact that we used a Malå Ramac antennae with a nominal frequency of 1.6 GHz, we clearly see that the center frequency is far from 1.6 GHz, due to antenna coupling, Debye dispersion and the dielectric permittivity gradient inside the column sand.

Graphics presented in Figure 14-a) and b) are the analog of Figure 13-a) and b) for the one-step experiment. The level of water is brought down to 0 cm from 71 cm (saturated) and then brought back to full saturation of the large tank. We see that the TWT of

the bottom reflection on Figure 13-b) exhibits the same behavior as the simulated one presented in Figure 3-b).

4.4. Inversion of Experimental Data

4.4.1. Frequency shift correction

The frequency shift observed in the experimental data (Figure 13-b) and Figure 14-b)) has to be taken into account in order to correct for the higher frequency picking, since all our TWT are relative to the saturated case (low frequency). Using the following procedure, we corrected the TWTs due the frequency variations during the experiment.

We considered that the wavelet associated with the bottom tank reflection could be assimilated as a time derived Ricker wavelet. We then measured the time delay between the maximum peak arrival of a wavelet computed with the lower frequency of 460 MHz (observed when the sand column is fully saturated), and the maximum peak arrival of a wavelet computed with the frequency associated with the experimental time at which we want to apply a correction. This principle is represented in Figure 15. Figure 15-b) represents the time correction with experimental time for the multi-step case. As expected, when the frequency difference between the initial measurement with the current one is larger the maximum time difference is larger. All numerical TWT were corrected using this procedure.

4.4.2. Data Inversion and Uncertainty Analysis with Bootstrapping

Using the same inversion loop as the one presented in the numerical case summarized in Figure 7, we inverted the experimental TWT data, sampled every 20 second, to obtain the hydrodynamic parameters of the considered soil. The parameters minimizing the objective function (Eq. 13) between the simulated and the experimental data are presented in

Table 2. We will present the uncertainty analysis only on two experiments, the multi-step experiment 15-01-26 and the One-step experiment 15-01-27. These two experiments will be further referred as multi-step and one-step experiment.

The uncertainty analysis was based on running multiple SCE-UA inversions on down-sampled data. This approach is similar to bootstrapping without replacement. For each experimental case, we chose randomly 50 sets of 80 points. For the multi-step data, we selected 40 points during the drainage and 40 point during the rewetting. For the mono-step data, we randomly took 60 points during drainage and 20 points during the rewetting phase. We performed inversions on each bootstrapped data subset. In each case, we selected the models with a RMSE value smaller than or equal to the RMSE of the best fitting model adding 10% to its value. Possible double models were taken out. It resulted into 231,192 parameter sets for the multi-step case and 238,432 parameter sets for the one-step case. The distributions of each model parameter are presented as histograms in Figure 16. These models are also displayed as objective function plots, Figure 17 and Figure 18, for the multi and one-step case respectively.

For each sub-figures (a) to k)) the parameter plane is label on x and y axis. For instance Figures 17-c) and 18-c) plots in the $\{\alpha_w, n\}$ plane all the models fitting the bootstrapped data with a RMSE value smaller than or equal to the one of the model optimizing the original data sampled at 20 s, plus 10%, for the multi-step and one-step experiment respectively. The colorbar in Figure 17-l) and Figure 18-l) represents the RMSE between modeled data and inversed data as computed from Eq. 13. The parameters fitting the HWC laboratory measurements are displayed as black points. K_s extreme values are represented by two black dashed lines as well as $\lambda = 0.5$. The optimum parameters (see

Table 2) obtained by inverting the original data sampled at 20 s are symbolized by black triangles.

4.5. Analysis of the Experimental Results

A look at the parameter sets obtained for the four different laboratory experiments, summed up in Table 2, shows differences in results that are hard to explain. We gain much more information looking at the histograms and the objective function plots issued from the bootstrapping analysis. The main differences between multi-step and one-step results concern the parameters λ and n.

The objective function plots including the λ parameter are in Figures 17-a), -d), -g) and -j) and 18-a), -d), -g) and -j). On Figure 17-a), we see that λ and n are correlated, with two regions of minimum RMSE around the points ($\lambda = 1$, $n = 3$) and ($\lambda = 9$, $n = 7$). This situation is similar to our previous analysis using Figure 10-g).

However, the WHC measurements indicate high value of n, even higher than the upper value found after bootstrapped data inversion. The WHC experiment is giving data at hydrostatic equilibrium. Therefore they do not involve hydraulic conductivity and the n parameter fitting these data is independent of the λ value. Considering the WHC results, the couple ($\lambda = 9$, $n = 7$) seems to be more reasonable than the couple ($\lambda = 1$, $n = 3$).

The one-step experiment is exploring directly the whole possible range of water saturation attainable in our 71 cm high column whereas the multi-step is cutting this range in four smaller ranges. It might explain why the one-step data fitting can not be achieved with small n, and small λ values (Figure 18-a)-d)-g)-j)).

If we exclude all the models with small n and λ values in Figure 17, all optimized parameters are in similar ranges in both experimental cases except for α_w (see histograms

of Figure 16). Figures 17 and 18 d) to f) show that K_s is very well defined, even if a small discrepancy is present, comparing to the measured data (Table 2).

Figures 17 and 18 h) show that the factor of two between α_d and α_w is more or less retrieved and no other correlation are found. In addition α_d seems to have a bi-modal shape over the two types of experiments, even if the separation between both peaks is quite small. Anyhow, both α_d and α_w are more efficiently retrieved in the one-step experiment than the multi-step one.

Diagrams on Figures 17 and 18 show us that θ_r, n and λ optimized parameters do not match the HWC parameters determined in the laboratory. At least two factors must be considered when comparing GPR-derived parameters and classical laboratory parameters. First, the parameters obtained in laboratory are made on 250 cm^3 core samples. Since about 330 kg of Fontainebleau sand were used in the large tank, the compaction was definitely not as homogeneous as in the case of small 250 cm^3 core samples, despite the fact that we tried to reach the same bulk density. In addition we are convinced that evaporation influenced the HWC measurements, which could explain the low θ_r values obtained with these experiments.

Second, the hydraulic head range covered by the HWC experiment is different than the one covered by the large scale experiment. Indeed, looking back at the HWC data presented in Figure 11, we see that the first drainage curve reaches 140 cm of suction, whereas in the case of our dynamical experiment we are dealing with at the most 70 cm. Then it is possible that we are not on the main wetting curve, but rather on an inner cycle curve. However this effect is taken into account by the hydrodynamical modeling.

5. Conclusion

The 1D velocity algorithm we used to invert the TWT from GPR data gave precise and accurate results for the numerical examples and allowed us to obtain most of the hydrodynamic parameters taking into account hysteresis in the water retention function.

Differences between the parameters obtained by our GPR experimental data inversion and those obtained through classical laboratory experiments (HWC and Ksat) are probably caused by homogeneity problems in the large tank and evaporation on the HWC soil samples. The hydraulic conductivity at saturation K_s is consistently estimated in all our bootstrapped data inversion into the range [0.8;1.2] cm.min^{-1}. The one-step experimental GPR data give more precise results than the multi-step experimental GPR data.

Values of λ between 6 and 10 and values of n between 4 and 7 were estimated from our GPR experiments. Both of these ranges are much higher than usually found in the literature for classical and/or specially designed laboratory experiments on soil samples [*Likos et al.*, 2013; *Abbasi et al.*, 2012; *Kumar et al.*, 2010]. These methods give dynamic volumetric water content data to be fitted using Equation (4), with the constrain on $\lambda = 0.5$. We tend to think that this constrain led to small n values. The parameter λ is important to retrieve, because it has a lot of influences on the other parameters to be estimated.

In the study presented here, the hysteresis of the water retention function is represented by the α parameter only. One of the possible improvement would be to give a higher degree of freedom by representing the hysteresis effect as well wit the θ_s, n and λ parameters.

Even if this work did not aim to study the efficiency of the empirical model of hysteresis used for the water retention function (model of *Kool and Parker* [1987]), we tend to think that other models should be tested. We particularly think that alternative models based

on contact angle-dependent hysteresis, such as the one of *Zhou* [2013], are very promising and may lead to a better physical representation of the hysteresis phenomena. However in this case the Richards' equation need to be solved by another code than the current version of Hydrus-1D.

Finally, the hydrodynamical parameters optimizing the TWT data would be better constrained using amplitudes of the reflections, particularly for the (n, λ) couple. That is why we encourage the development of a full-waveform inversion algorithm.

Acknowledgments. The authors thank the reviewers for their constructive remarks on the first version of this paper, as well as Guillaume Giot and Isabelle Cousin from INRA Orléans for their measurements of the hydraulic conductivity at saturation on sand samples. All data are available upon request from the corresponding author.

References

Abbasi, F., M. Javaux, M. Vanclooster, and J. Feyen (2012), Estimating hysteresis in the soil water retention curve from monolith experiments, *Geoderma*, *189*, 480–490.

Akbar, M., A. Kenimer, S. Searcy, and H. Tobert (2005), Soil water estimation using electromagnetic induction, *Trans. ASAE*, *48*(1), 129–135.

Alharthi, A., and J. Lange (1987), Soil water saturation: Dielectric determination, *Water Resour. Res.*, *23*(4), 591–595.

Annan, A. (1999), Ground Penetrating Radar: Workshop notes, *Tech. rep.*, Sensors and Software Inc., Ontario, Canada.

Birchak, J., L. Gardner, J. Hipp, and J. Victor (1974), High dielectric constant microwave probes for sensing soil moisture, *Proceedings IEEE*, *35*(1), 85–94.

Brooks, R., and A. Corey (1964), Hydraulic properties of porous media, *Hydrol. pap. 3*, Colo. State Univ., Fort Collins, Colo.

Burdine, N. (1953), Relative permeability calculations from pore-size distribution data, *Journ. Petr. Tech.*, *5*(3), 71–77.

Cai, J., and G. A. McMechan (1995), Ray-based synthesis of bistatic Ground-Penetrating Radar profiles., *Geophysics*, *60*(1), 87–96.

Collis-George, N. (1955), Hysteresis in moisture content-suction relationships in soils, *Proc. Nat. Acad. Sci.*, *24A*, 80–85.

Dagenbach, A., J. Buchner, P. Klenk, and K. Roth (2013), Identifying a parametrisation of the soil water retention curve from on-ground GPR measurements., *Hydrol. Earth Syst. Sci.*, *17*(1), 611–618.

Dane, J. H., and J. W. Hopmans (2002), *Method of soil analysis, Part 4, Physical methods*, chap. Hanging water column, pp. 680–684, Soil Science Society of America, Inc., Madison, WI.,USA.

Debye, P. (1929), *Polar Molecules*, Dover Publications, New York.

Diamanti, N., and A. A. J. Redman (2014), Impact of gradational electrical properties on GPR detection of interfaces, in *Ground Penetrating Radar (GPR), 2004 15th International Conference on*, pp. 529–534, IEEE.

Duan, Q., S. Sorooshian, and V. Gupta (1992), Effective and efficient global optimization for conceptual rainfall-runoff models, *Water Resour. Res.*, *28*(4), 1015–1031.

Eching, S., and J. Hopmans (1993), Optimization of hydraulic functions from transient outflow and soil water pressure data, *Soil Sci. Soc. Am. J.*, *57*(5), 1167–1175.

Eching, S., J. Hopmans, and O. Wendroth (1994), Unsaturated hydraulic conductivity from transient multistep outflow and soil water pressure data, *Soil Sci. Soc. Am. J.*, *58*(3), 687–695.

Efron, B. (1979), Bootstrap methods: another look at the jackknife, *The annals of Statistics*, pp. 1–26.

Enderby, J. (1955), The domain model of hysteresis, *Trans. Faraday Soc.*, *51*, 835–848.

Endres, A., W. Clement, and D. Rudolph (2000), Ground penetraing radar imaging of an aquifer during a pumping test, *Ground Water*, *38*, 566–576.

Everett, D. (1954), A general approach to hysteresis, part 3: a formal treatment of the independent domain model of hysteresis, *Trans. Faraday Soc.*, *50*, 1077–1096.

Everett, D. (1955), A general approach to hysteresis, 4, *Trans. Faraday Soc.*, *51*, 1551–1557.

Everett, D., and W. Whitton (1952), A general approach to hysteresis, *Trans. Faraday Soc.*, *48*, 749–757.

Fleury, M., and D. Longeron (1998), Combined resistivity and capillary pressure measurments using micropore membrane technique, *Journal of Petroleum Science & Engineering*, *19*, 73–79.

Fredlung, D., and A. Xing (1994), Equations for the soil-water characteristic curve, *Can. Geotech. J.*, *31*(4), 521–532.

Fuentes, C., R. Haverkamp, and J. Parlange (1992), Parameters constraints on closed-form soil water relationships, *J. Hydrol.*, *134*(1-4), 117–142.

Gardner, W. (1958), Some steady state solutions of the unsaturated moisture flow equation with application to evaporation for a water table, *Soil Sci.*, *85*, 228–233.

661 Giannopoulos, A. (2005), Modelling Ground-Penetrating Radar by GprMax, *Constr.*
662 *Build. Mater.*, *19*(10), 755–762.

663 Goyal, V., P. Gupta, S. Seth, and V. Singh (2006), Estimation of temporal changes in soil
664 moisture using resistivity method, *Hydrol. Process.*, *10*(9), 1147–1154.

665 Haines, W. (1930), Studies in the physical properties of soils: 5 the hysteresis effect in
666 capillary properties and the modes of moisture distribution associated therewith, *J.*
667 *Agr. Sci.*, *20*, 91–116.

668 Haverkamp, R., F. Leij, C. Fuentes, A. Sciortino, and P. Ross (2005), Soil water retention:
669 I. introduction of a shape index, *Soil Sci. Soc. Am. J.*, *69*(6), 1881–1890.

670 Hopmans, J., and J. Dane (1986), Temperature dependence of soil hydraulic properties,
671 *Soil Sci. Sco. Am. J.*, *50*(1), 4–9.

672 Hubbard, S., and Y. Rubin (2000), Hydrogeological parameter estimation using geophys-
673 ical data: A review of selected techniques, *Journal of Contam. Hydrol.*, *45*(1-2), 1623–
674 1630.

675 Huisman, J., S. Hubbard, J. Redman, and A. Annan (2003), Measuring soil water content
676 with Ground-Penetrating Radar., *Vadose Zone J.*, *2*(4), 476–491.

677 Irving, J., and R. Knight (2006), Numerical modeling of Ground-Penetrating Radar in
678 2D using Matlab, *Comput. Geosci.*, *32*(9), 1247–1258.

679 Klein, L., and C. Swift (1977), An improved model for the dielectric constant of sea water
680 at microwave frequencies, *IEEE Trans. Geosci. Remote Sens.*, *25*(1), 104–111.

681 Klenk, P., S. Jaumann, and K. Roth (2015), Quantitative high-resolution observations of
682 soil water dynamics in a complicated architecture using time-lapse ground-penetrating
683 radar, *Hydrol. Earth Syst. Sci.*, *19*, 1125–1139.

Knight, R. (1991), Hysteresis in the electrical resistivity of partially saturated sandstones, *Geophysics*, *56*(12), 2139–2147.

Knight, R., and A. Abad (1995), Rock/water interaction in dielectric properties: Experiments with hydrophobic sandstones, *Geophysics*, *60*(2), 431–436.

Knight, R., E. Grunewald, T. Irons, K. Dlubac, Y.-Q. Song, H. Bachman, B. Grau, D. Walsh, J. Abraham, and J. Cannia (2012), Field experiment provides ground truth for surface NMR measurement, *Geophy. Res. Lett.*, *39*(3).

Knoll, M. (1996), Petrophysical basis for ground penetrating radar and very early time electromagnetics: Electrical properties of sand-clay mixtures, Ph.D. thesis, University of British Columbia, Vancouver.

Kool, J., and J. Parker (1987), Development and evaluation of closed-form expressions for hysteretic soil hydraulic properties, *Water Resour. Res.*, *23*(1), 105–114.

Kosugi, K., J. Hopmans, and J. Dane (2002), *Methods of Soil Analysis, Part 4, Physical Methods*, chap. Parametric Models, pp. 739–755, Soil Science Society of America,Inc., Madison, WI.

Kowalsky, M., P. Dietrich, G. Teutsch, and Y. Rubin (2001), Forward modeling of Ground-Penetrating Radar using digitized outcrop images and multiple scenarios of water saturation, *Water Resour. Res.*, *37*(6), 1615–1626.

Kumar, S., M. Sekhar, D. Reddy, and M. M. Kumar (2010), Estimation of soil hydraulyc properties and their uncertainty comparison between laboratory and field experiment, *Hydrol. Process.*, *24*, 3426–3435.

Kunz, K., and R. Luebbers (1993), *The Finite Difference Time Domain Method for Electromagnetics*, CRC Press.

Lai, W., W. Tsang, H. Fang, and D. Xiao (2006), Experimental determination of bulk dielectric properties and porosity of porous asphalt and soils using GPR and a cyclic moisture variation technique, *Geophysics*, *71*(4), K93–K102.

Leij, F., R. Haverkamp, C. Fuentes, F. Zatarain, and P. Ross (2005), Soil water retention: Ii derivation and application of shape index, *Soil Sci. Sco. Am. J.*, *69*, 1891–1901.

Lesmes, D., and S. Friedman (2005), *Hydrogeophysics*, chap. Relationship between the electrical and hydrogeological properties of rocks and soils, Springer.

Likos, W. J., N. Lu, and J. W. Godt (2013), Hysteresis and uncertainty in soil water-retention curve parameters, *Journal of Geotechnical and Geoenvironmental Engineering*.

Morow, N., and C. Harris (1965), Capillary equilibrium in porous materials, *Soc. Petrol. Eng. J.*, *5*, 15–24.

Moss, A., X. Jing, and J. Archer (1999), Laboratory inverstigation of wettability and hysteresis effects on resistivity index and capillary pressure characteristics, *Journal of Petroleum Science & Engineering*, *24*, 231–242.

Mualem, Y. (1973), Modified approach to capillary hysteresis based on a similarity hypothesis, *Water Resour. Res.*, *9*(5), 1324–1331.

Mualem, Y. (1974), A conceptual model of hysteresis, *Water Resour. Res.*, *10*(3), 514–520.

Mualem, Y. (1976), A new model for predicting the hydraulic conductivity of unsaturated porous media., *Water Resour. Res.*, *12*(3), 513–522.

Mualem, Y. (1977), Extension of the similarity hypothesis used for modeling the soil water characteristics, *Water Resour. Res.*, *13*(4), 773–780.

Mualem, Y. (1984), A modified dependent-domain theory of hysteresis, *Soil Sci.*, *137*(5), 283–291.

730 Mualem, Y., and G. Dagan (1975), A dependent domain model of capillary hysteresis in
731 porous materials, *Water Resour. Res.*, *11*(3), 452–460.
732 Néel, L. (1942), Théorie des lois d'aimantation de Lord Rayleigh, 1, *Cahiers Phys.*, *12*,
733 1–20.
734 Néel, L. (1943), Théorie des lois d'aimantation de Lord Rayleigh,2, *Cahiers Phys.*, *13*,
735 18–30.
736 Peters, A., and W. Durner (2008), Simplified evaporation method for determining soil
737 hydraulic properties, *J. Hydrol.*, *356*(1), 147–162.
738 Philip, J. (1964), Similarity hypothesis for capillary hysteresis in porous materials, *J.*
739 *Geophys. Res.*, *69*(8), 1553–1562.
740 Poulovassilis, A. (1962), Hysteresis of pore water, an application of the concept of inde-
741 pendent domains, *Soil Sci.*, *93*, 405–412.
742 Poulovassilis, A. (1970), Hysteresis of pore water in granular porous bodies, *Soil Sci.*, *109*,
743 5–12.
744 Preisach, F. (1935), Ubcurve magnetische nachwirkung, *Z. Physik*, *94*, 277–302.
745 Richards, L. (1931), Capillary conduction of liquids through porous mediums, *J. Appl.*
746 *Phys.*, *1*(5), 318–333.
747 Roth, K., R. Schulin, H. Flühler, and W. Attinger (1990), Calibration of time domain
748 reflectometry for water content measurement using a composite dielectric approach,
749 *Water Resour. Res.*, *26*(10), 2267–2273.
750 Saintenoy, A., and J. Hopmans (2011), Ground Penetrating Radar: Water table detection
751 sensitivity to soil water retention properties, *IEEE J. Sel. Topics Appl. Earth Observ.*
752 *in Remote Sens.*, *4*(4), 748–753.

753 Schaap, M., and F. Leij (2000), Improved prediction of unsaturated hydraulic conductivity
754 with the mualemÂśvan genuchten model, *Soil Sci. Soc. Am. J.*, *62*, 843–851.
755 Schaap, M., and M. van Genuchten (2005), A modified Mualem-van Genuchten formu-
756 lation for improved description of the hydraulic conductivity near saturation, *Vadose*
757 *Zone Journal*, *5*, 27–34.
758 Schaap, M., J. Feike, and M. van Genuchten (2001), ROSETTA: a computer program for
759 estimating soil hydraulic parameters with hierarchical pedutransfert functions, *Journal*
760 *of Hydrology*, *251*, 163–176.
761 Scott, P., G. Farquhar, and N. Kouwen (1983), *Hysteretic effects on net infiltration, Ad-*
762 *vances in infiltration*, vol. 11-83, chap. Advances in infiltration, pp. 163–170, Am. Soc.
763 Agric. Eng.
764 Sethian, J., and A. Popovici (1999), 3-D travel time computation using the fast marching
765 method, *Geophysics*, *64*(2), 516–523.
766 Sheets, K., and J. Hendrickx (1995), Non invasive soil water content measurement using
767 electromagnetic induction, *Water Resour. Res.*, *31*(10), 2401–2409.
768 Shivola, A. (1999), *Electromagnetic mixing formulas and applications*, vol. 47, Electro-
769 magnetic Waves Series, London.
770 Šimunek, J., R. Kodešovà, M. Gribb, and M. van Genuchten (1999), Estimating hysteresis
771 in the soil water retention function from cone permeameter experiments, *Water Resour.*
772 *Res.*, *35*(5), 1329–1345.
773 Šimunek, J., M. T. van Genuchten, and M. Sejna (2008), Development and applications
774 of the HYDRUS and STANMOD software packages, and related codes, *Vadose Zone*
775 *J.*, *7*(2), 587–600.

Stogryn, A. (1971), Equations for calculating the dielectric constant of saline water, *IEEE Trans. Microw. Theory Tech.*, *MTT-19*(8), 733–736.

Talsma, T. (1970), Hysteresis in two sands and independent domain model, *Water Resour. Res.*, *6*(3), 964–970.

Topp, G. (1969), Soil water hysteresis measured in sandy loam compared with the hysteric domain model, *Soil Sci. Sco. Am. J.*, *33*, 645–651.

Topp, G. (1971), Soil water hysteresis in silt loam and clay loam soils, *Water Resour. Res.*, *7*(4), 914–920.

Topp, G., and E. Miller (1966), Hysteretic moisture characteristics and hydraulic conductivities for glass-bead media, *Soil Sci. Soc. Am. J.*, *30*(2), 156–162.

Tsolfias, G., T. Halihan, and J. S. Jr. (2001), Monitoring pumping test response in a fractured aquifer using ground-penetrating radar, *Water Resour. Res.*, *37*, 1221–1229.

Vachaud, G., and J. Thony (1971), Hysteresis during infiltration and redistribution in a soil column at different initial water contents, *Water Resour. Res.*, *7*, 111–127.

van Genuchten, M. T. (1980), A closed form equation for predicting the hydraulic conductivity of unsaturated soils, *Soil Sci. Soc. Am. J.*, *44*(5), 892–898.

Vereecken, H., J. Huisman, H. Bogena, and J. Vanderborght (2008), On the value of soil moisture measurements in vadose zone hydrology: A review, *Water Resour. Res.*, *44*(4), 1–21.

Vrugt, J., H. Gupta, W. Bouten, and S. Sorooshian (2003), A Shuffled Complex Evolution Metropolis algorithm optimization and uncertainty assesment of hydrologic models parameters, *Water Resour. Res.*, *39*(8).

Weihnacht, B., and F. Boerner (2014), Measurement of retention functions with hysteresis using ground-penetrating radar, *Near Surf. Geophys.*, *12*, 539–548.

Wind, G. P. (1966), Capillary conductivity data estimated by a simple method, in *Proceedings of the Wageningen Symposium - Water in the unsaturated zone*, edited by I. A. of Scientific Hydrology, pp. 182–191.

Wösten, J., A. Lilly, A. Nemes, and C. L. Bas (1999), Development and use of a database of hydraulic properties of European soils, *Geoderma*, *90*, 169–185.

Zhou, A.-N. (2013), A contact angle-dependent hysteresis model for soil-water retention behaviour, *Comput. Geotech.*, *49*, 36–42.

Zhou, Q., J. Shimada, and A. Sato (2001), Three-dimensionnal spatial and temporal monitoring of soil water content using electrical resistivity tomography, *Water Resour. Res.*, *37*(2), 273–285.

	θ_r ($cm^3.cm^{-3}$)	θ_s ($cm^3.cm^{-3}$)	α^d (cm^{-1})	α^w (cm^{-1})	n	K_s (cm/min)	λ	RMSE (ns)
$\boldsymbol{p_{in}}$	0.05	0.35	0.025	0.05	6	1	0.5	-
multi-step - heads $= [71; 42; 32; 23; 0; 23; 32; 42; 71]$ cm								
$\boldsymbol{p_{MS}^{op}}$	0.048	0.38	0.024	0.052	5.29	1.08	0.55	0.014
one-step - heads $= [71; 0; 71]$ cm								
$\boldsymbol{p_{OS}^{op}}$	0.056	0.38	0.024	0.053	6.06	1.08	0.54	0.013

Table 1. Hydrodynamical M-vG parameters of the numerical experiments. p_{in} is the set of parameters used as input to generate the radargrams presented in Figures 4-a) and 4-b). The set of parameters optimized by the SCE-UA global method is p_{MS}^{op} in the multi-step case and p_{OS}^{op} in the one-step case.

	θ_r ($cm^3.cm^{-3}$)	θ_s ($cm^3.cm^{-3}$)	α^d (cm^{-1})	α^w (cm^{-1})	n	K_s^* (cm/min)	λ^{**}	RMSE (ns)
Lab. meas.	0.03 ± 0.005	0.36 ± 0.005	0.024 ± 0.002	0.043 ± 0.003	8.5 ± 0.5	$[0.96; 1.5]$	0.5	-
multi-step - heads $= [71; 41.5; 31.5; 22.5; 0; 22.5; 31.5; 41.5; 71]$ cm								
15-01-26	0.052	0.37	0.033	0.094	6.6	0.82	10.4	0.14
15-01-20	0.04	0.36	0.023	0.047	4.4	0.54	0.25	0.09
one-step - heads $= [71; 0; 71]$ cm								
15-01-23	0.045	0.40	0.023	0.052	5.52	0.90	4.9	0.149
15-01-27	0.04	0.4	0.028	0.042	5.14	0.88	8.54	0.148

Table 2. Hydrodynamical M-vG parameter sets from classical laboratory measurements and optimizing laboratory GPR data monitoring. * obtained from Ksat. ** according to *Mualem* [1976].

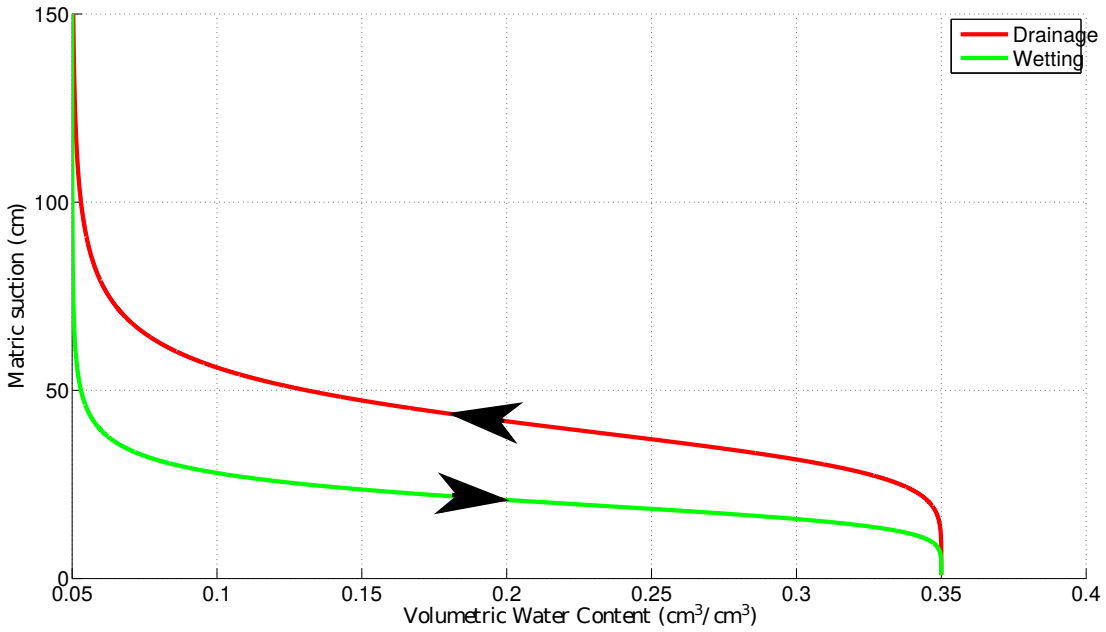

Figure 1. The red curve is the main drying curve, the green is the main wetting curve. The black arrow symbolizes the direction of the cycle. The hysteresis is only determined by the α parameters, with $\alpha_w = 2\alpha_d$. See Table 1 for the full parameter set.

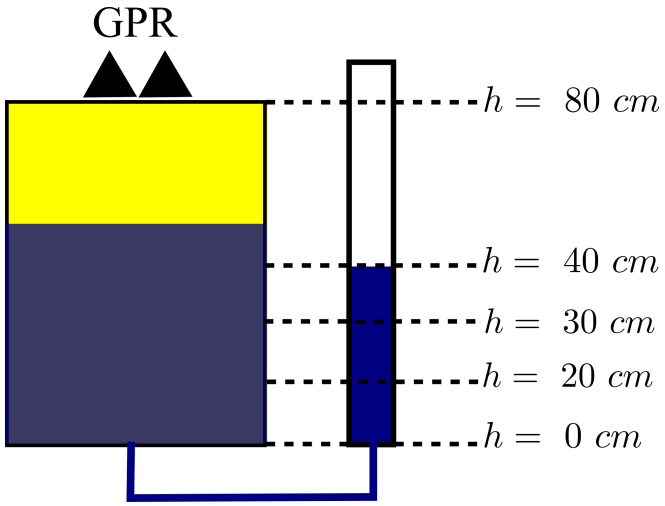

Figure 2. Draft of the experiment. The tank is 80 cm high and filled with sand. The small diameter reservoir on the right represent the different heads applied at the bottom of the tank. GPR antennae are set on top of the sand reservoir.

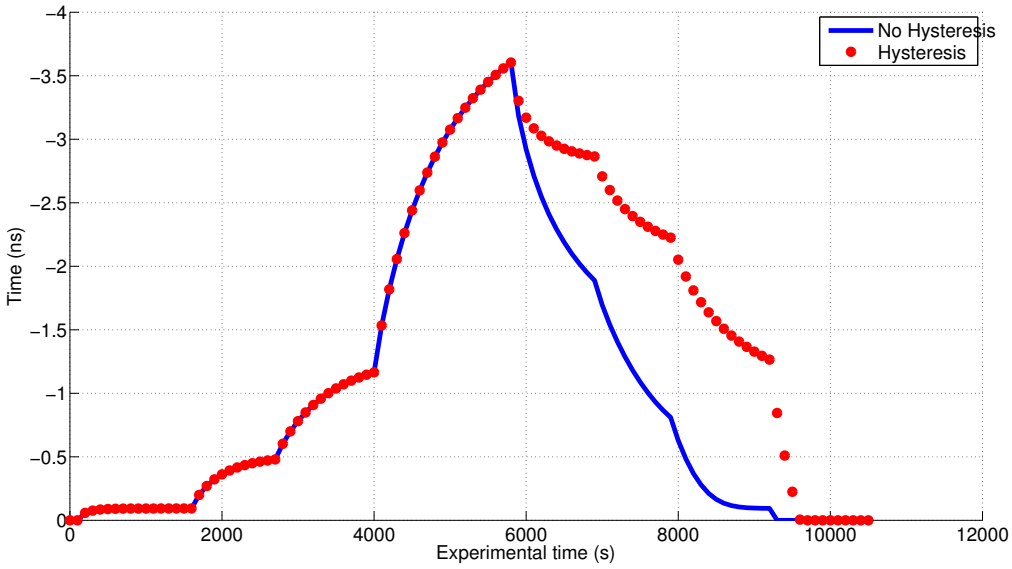

a)

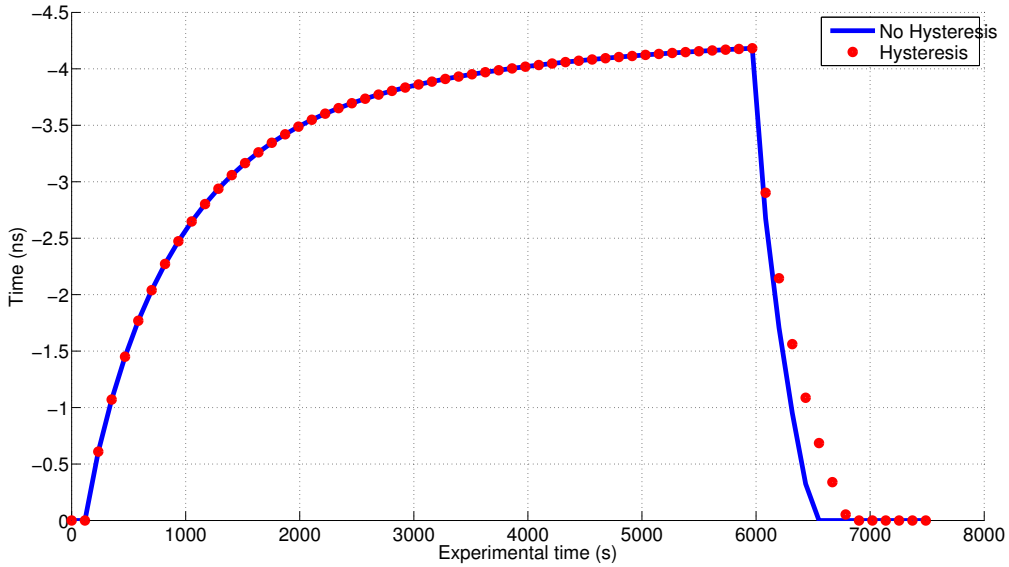

b)

Figure 3. TWT of the bottom tank reflection. a): The heads applied at the bottom boundary condition were 71 cm (saturated)-42-32-23-0 cm, then re-wetting following the same steps. b) The heads applied were 71 cm (saturated)-0 cm, then re-wetting to 71 cm. Blue curves represent the computed TWT using a hydrodynamic function without taking into account hysteresis effects, whereas the red circles are modeled using hysteresis. The parameters used for the hydrodynamical modeling are presented in Table 1.

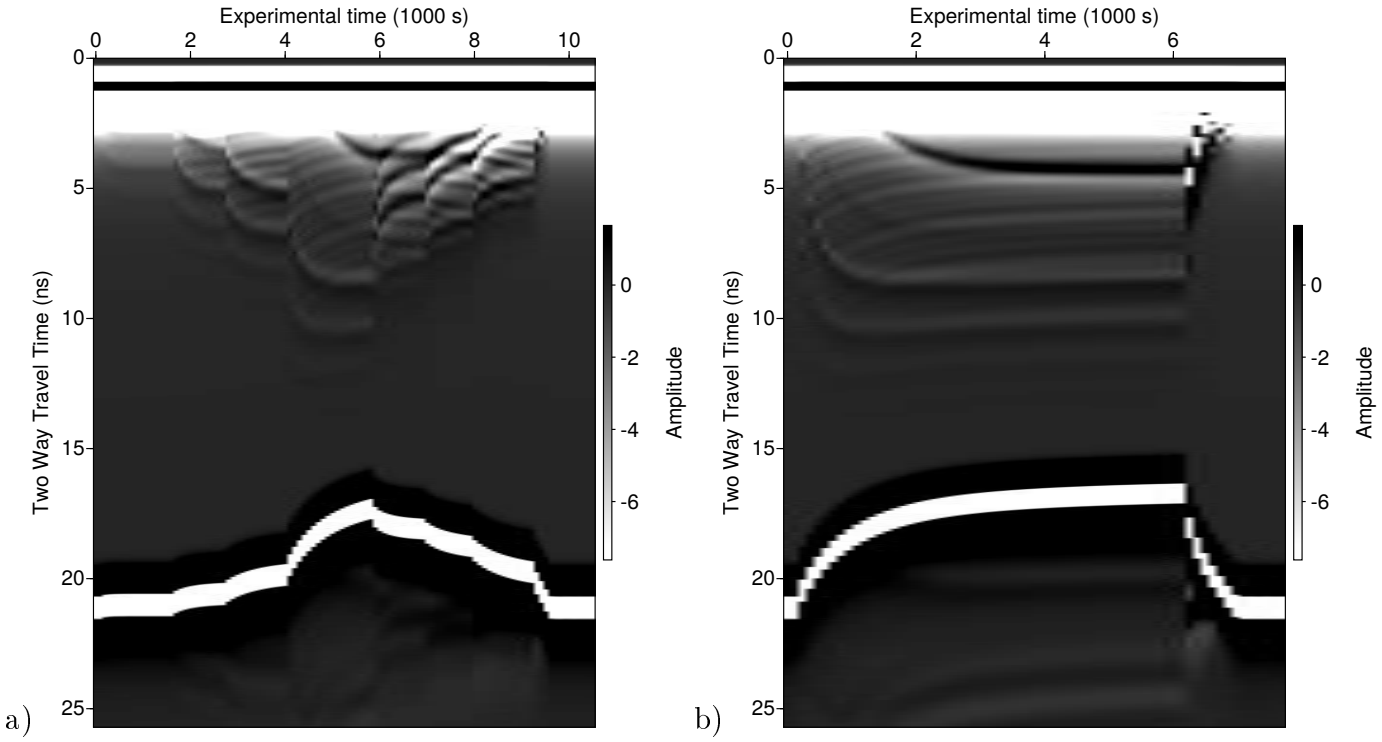

Figure 4. Radargrams generated from the simulated water content profiles using GprMax2D: a) multi-step experiment b) one-step experiment. The parameters used as input for the hydrodynamical modeling are presented in Table 1.

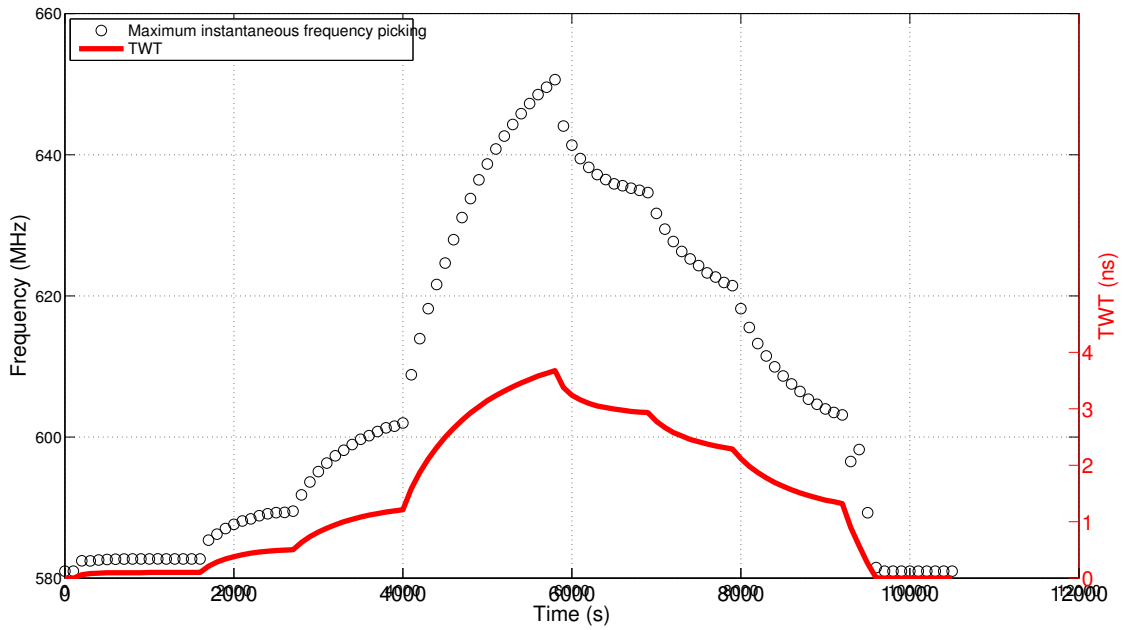

a)

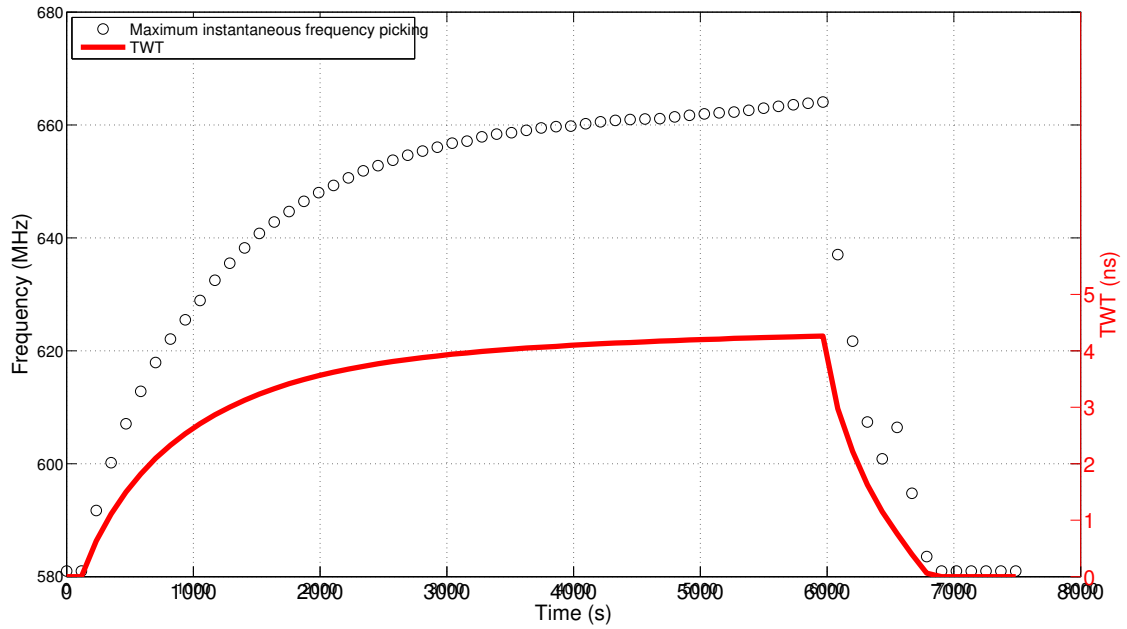

b)

Figure 5. Maximum frequency of the bottom tank reflection for a) multi-step and b) one-step experiment. Automatically picked maximum instantaneous frequency from the signal at the bottom of the tank (circles), TWT relative to the initial state (red line).

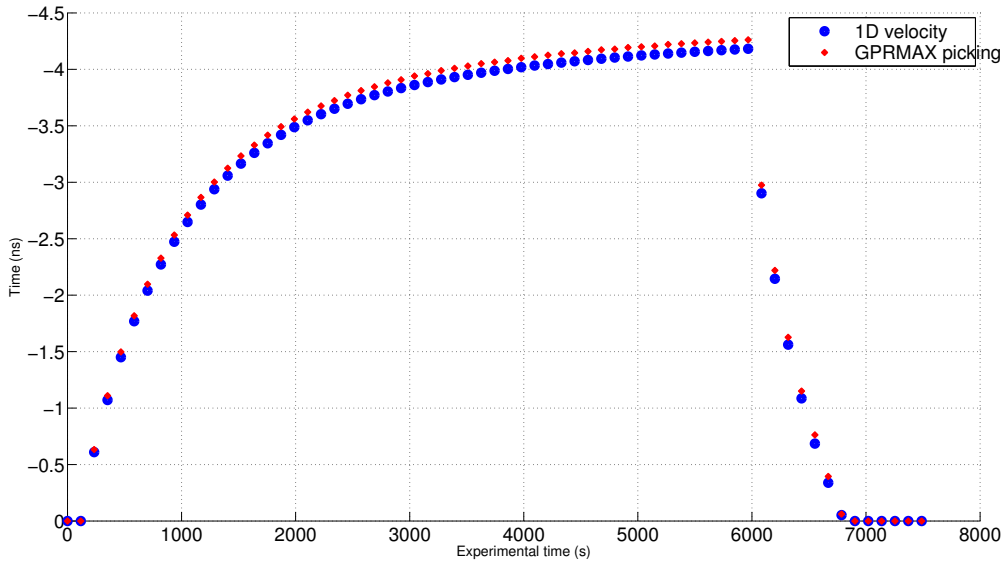

a)

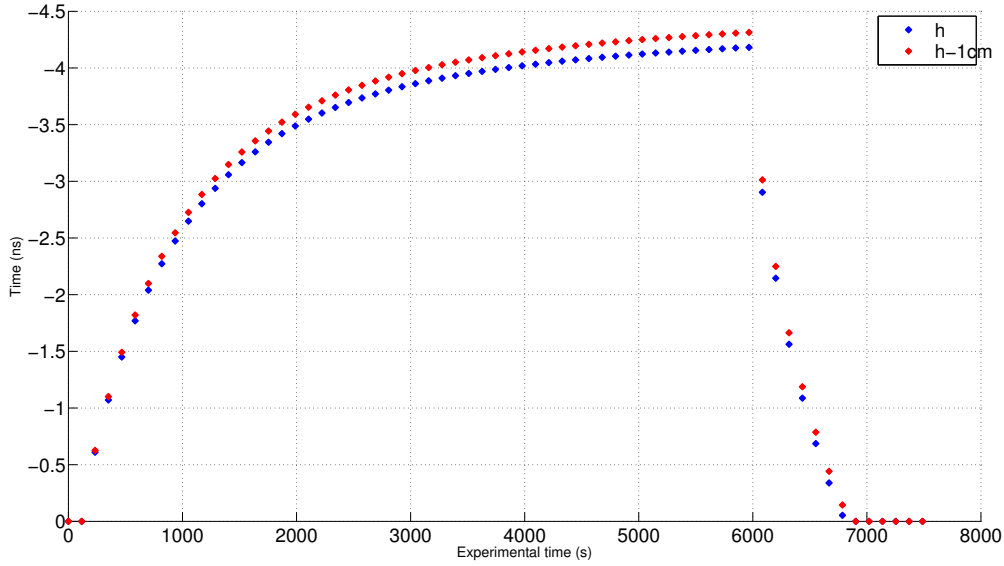

b)

Figure 6. TWT from the bottom tank reflection, relative to the initial saturated case, for the one-step case. a) Comparison between the TWT computed using our simple 1D-velocity modeling (blue dots) and the TWT picked in the GPRMAX2D radargram (red dots). These differences (RMSE=0.09 ns) are due to frequency dispersion, taken into account in GPRMAX2D but not in our 1D modeling. b) Comparison between the TWT computed using our simple 1D-velocity with the hydraulic heads presented in Table 1 (blue dots), and with the hydraulic heads decreased by 1 cm (red dots). The RMSE associated with this discrepancy is 0.11 ns.

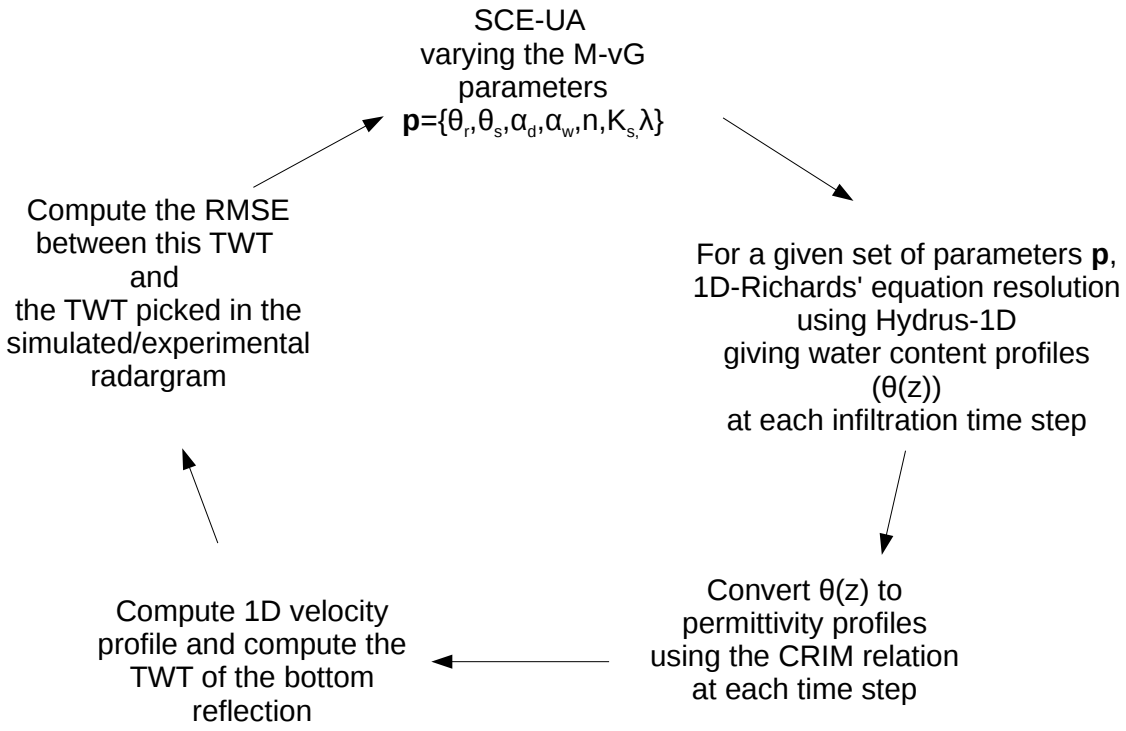

Figure 7. Flow diagram of the inversion procedure. "SCE-UA": Shuffled Complex Algorithm, "M-vG": Mualem-van Genuchten, "CRIM": Complex Refractive Index Method, "TWT": Two Way Travel-time, "RMSE": Root Mean Squared Error.

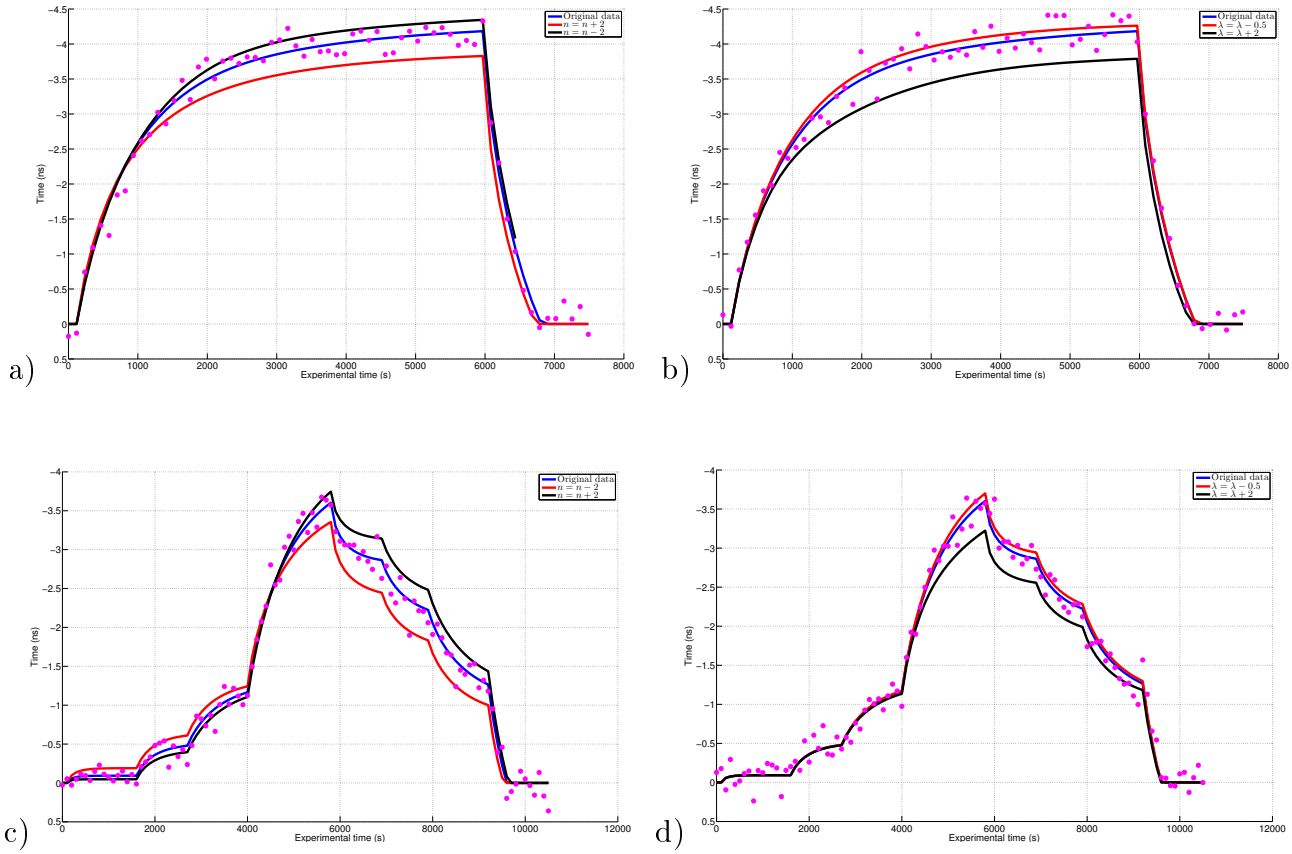

Figure 8. TWT with input parameters (Table 1) in blue, red and black curves represent TWT computed with different n values (one-step in a) and multi-step case in c)) and λ values (one-step in b) and multi-step case in d)). Purple points are the perturbed input data adding noise sampled in a Gaussian distribution with standard deviation 0.13 ns for the multi-step case and 0.15 ns for the one-step case.

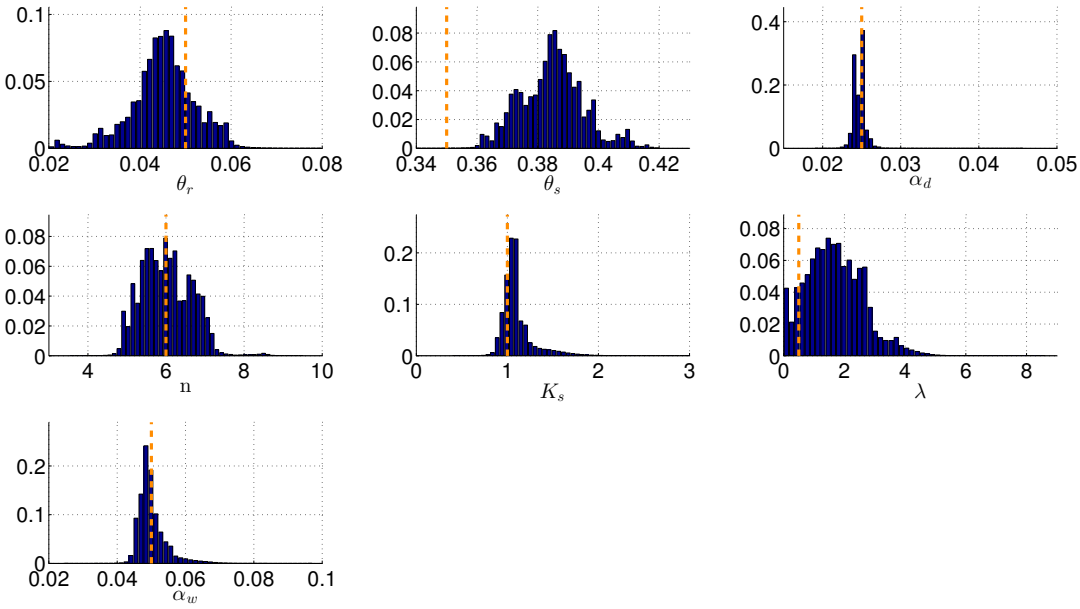

a)

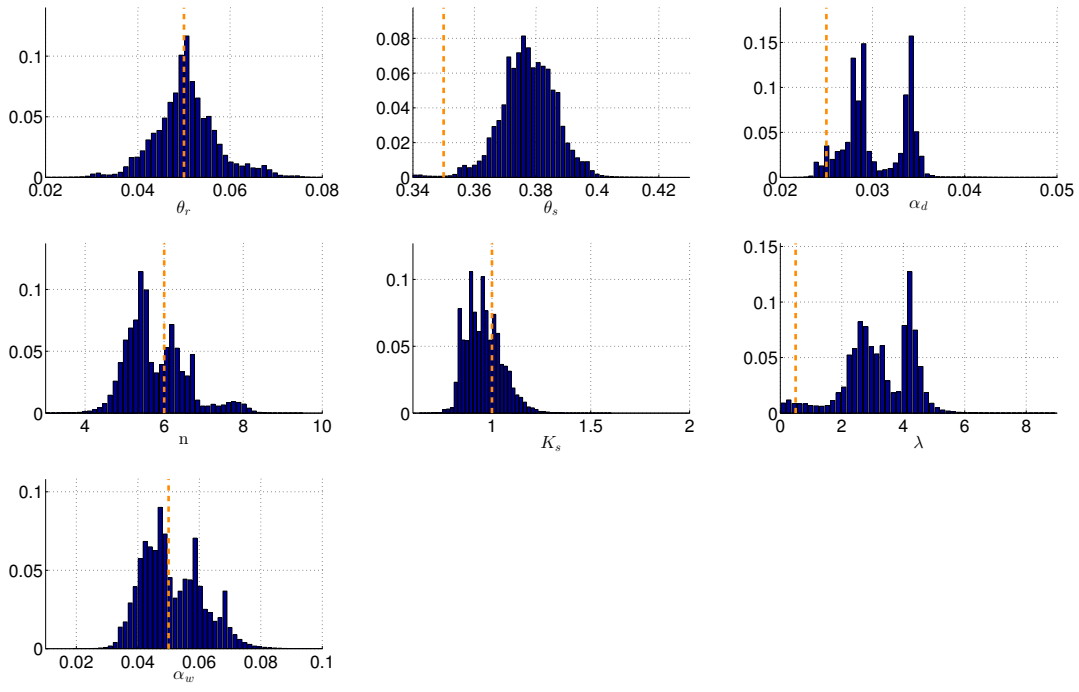

b)

Figure 9. Histograms realized on models fitting simulated data, a) in the multi-step case, presented on radargram 4-a), b) in the one-step case, presented on radargram 4-b). For each model the RMSE is smaller than 2σ (0.26 ns in the multi-step case and 0.3 ns in the one-step case). The orange vertical lines symbolize the values used as input parameters.

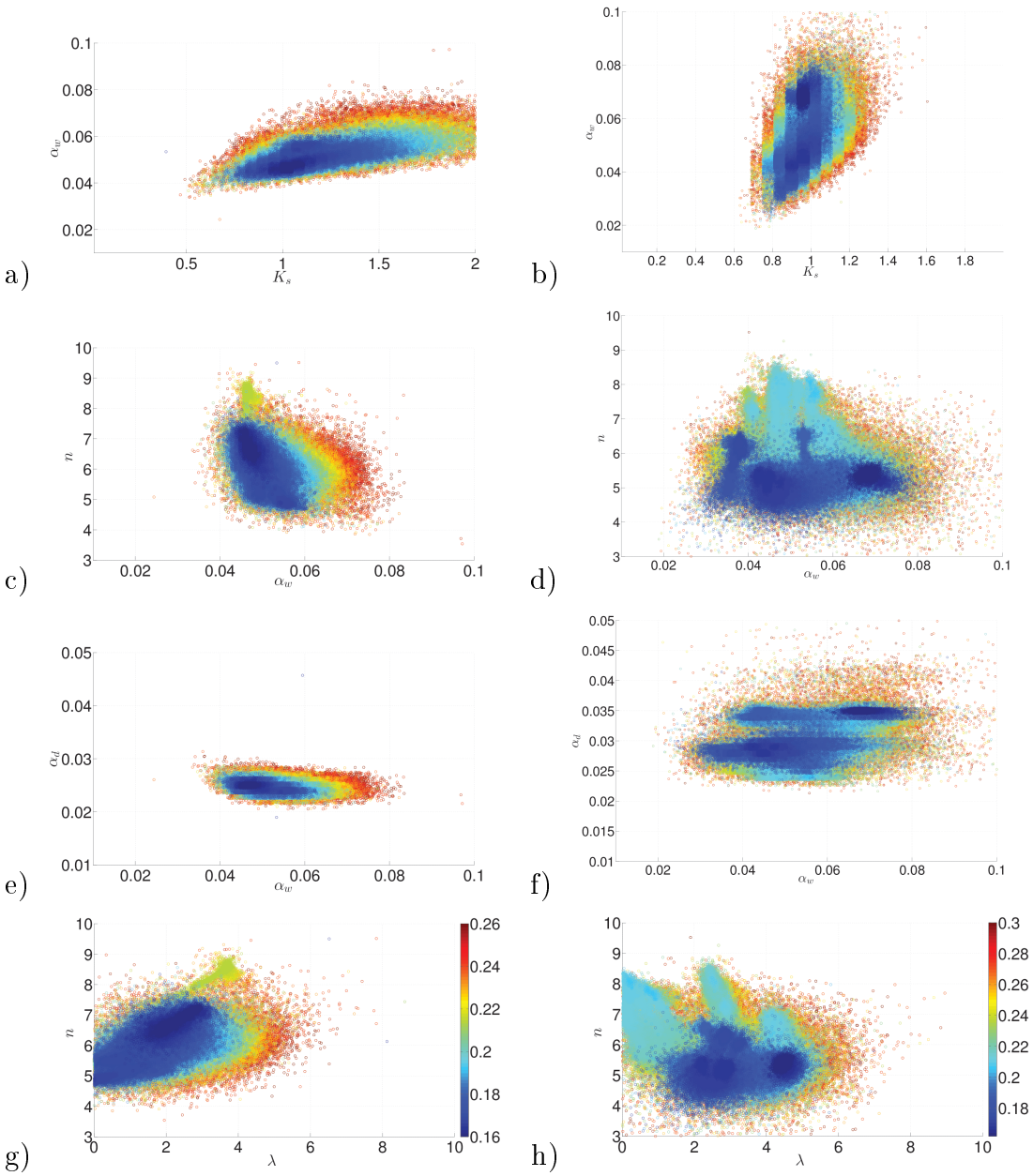

Figure 10. Objective function plots realized on noise-added simulated data keeping all parameter sets giving a RMSE value smaller or equal than 2σ. Diagrams in the left column (a, c, e and g) were computed for the multi-step case while those in the right column (b, d, f and h) were computed for the one-step case. The color bars displayed in g) and h) are RMSE (ns) and are valid for all objective function plots in each column.

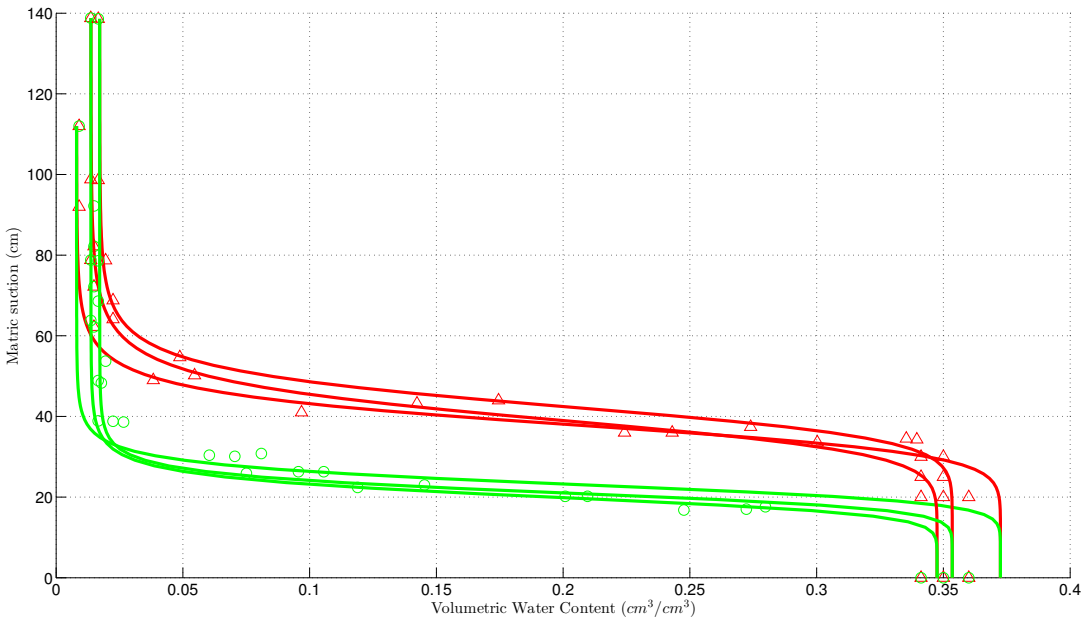

Figure 11. Results of water hanging column experiments including a drying and wetting cycle. Samples were prepared with the same bulk density as the sand in the cylindrical tank experiment. Red triangles: drying data; green circles: wetting data. Plain curves represent the model fitting the data with the parameters p_{lab} in Table 2.

Figure 12. Pictures of the experiments. On the left is presented the tank filled with water, with its overflow connections. Middle picture shows the tubing linking both tanks. The picture on the right displays the sand tank with the GPR set at the top with a load on it.

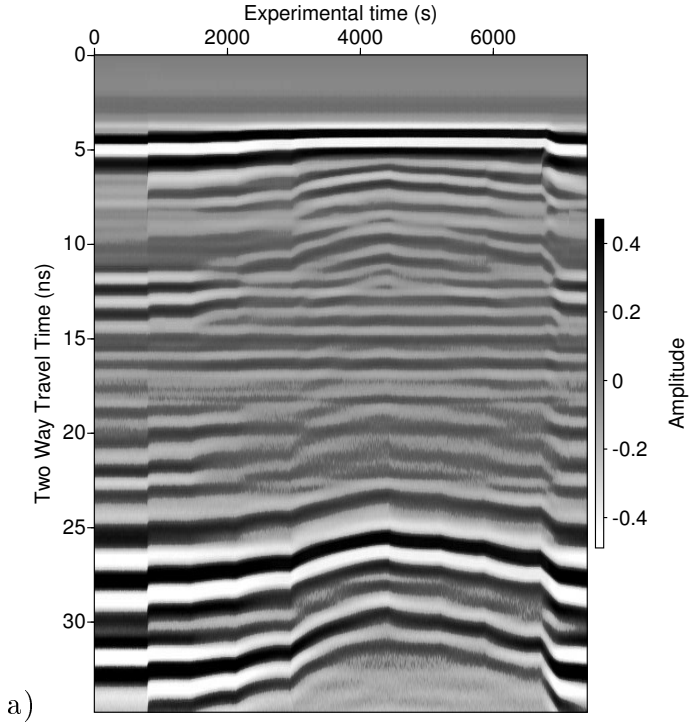

a)

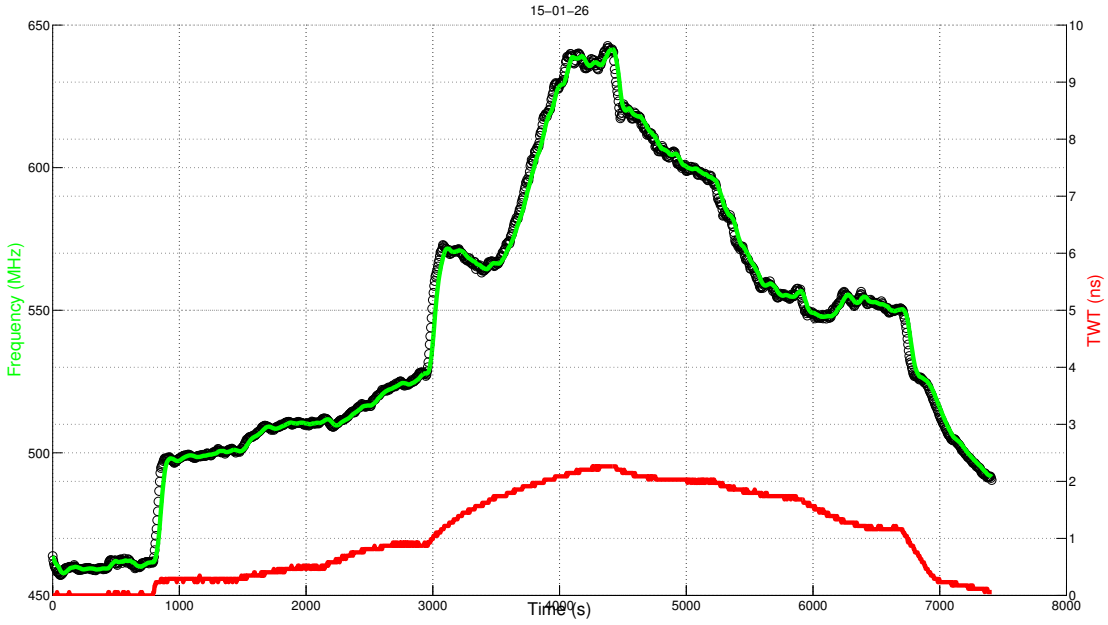

b)

Figure 13. a) Radargram acquired along a multi-step experiment. The reflection coming from the bottom of the tank is arriving between 25 and 30 ns. Other reflections are coming from tank edges and the capillary fringe. b) Maximum frequency of the reflection at the bottom of the tank (circles), after moving window averaging (green plain line), TWT relative to its initial value (red line).

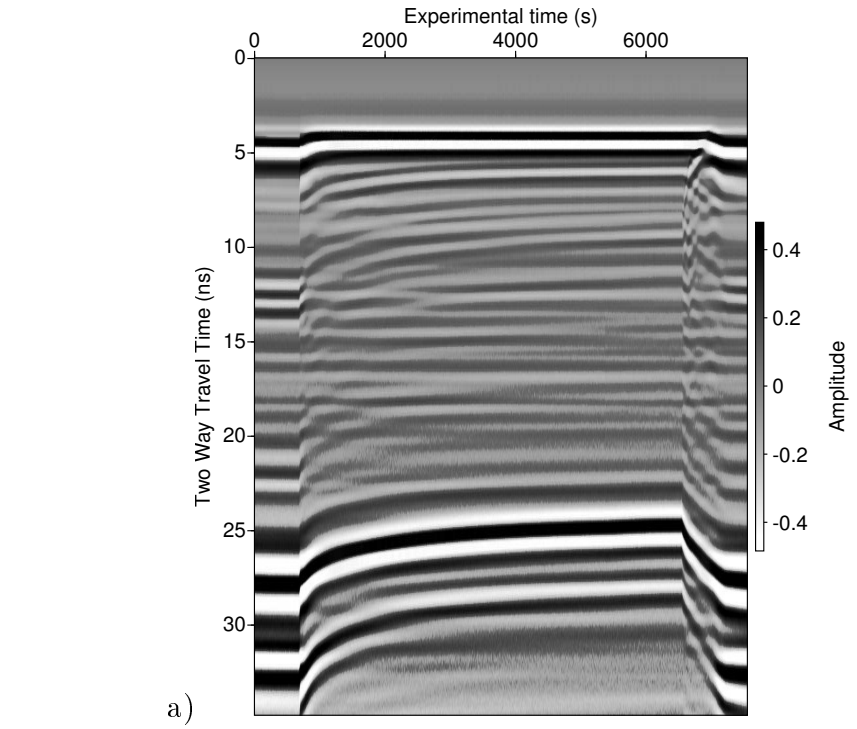

a)

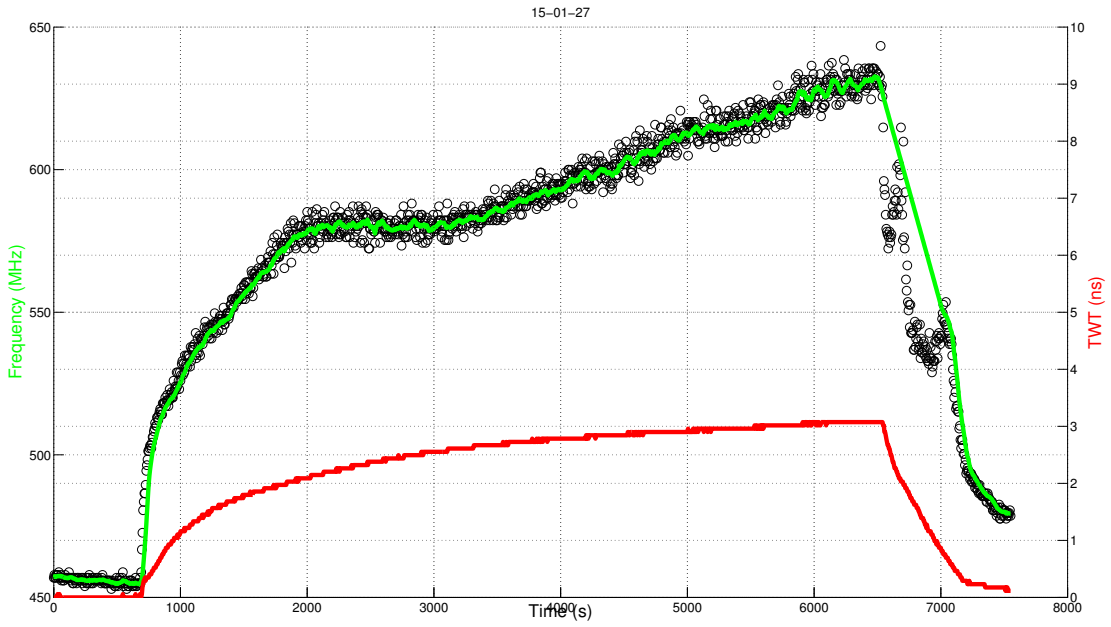

b)

Figure 14. a) Radargram acquired along a one-step experiment. The reflection coming from the bottom of the tank is arriving between 25 and 30 ns. Other reflections are coming from tank edges and the capillary fringe. b) Maximum frequency of the reflection at the bottom of the tank (circles), after moving window averaging and manual correction (green plain line), TWT relative to its initial value (red line).

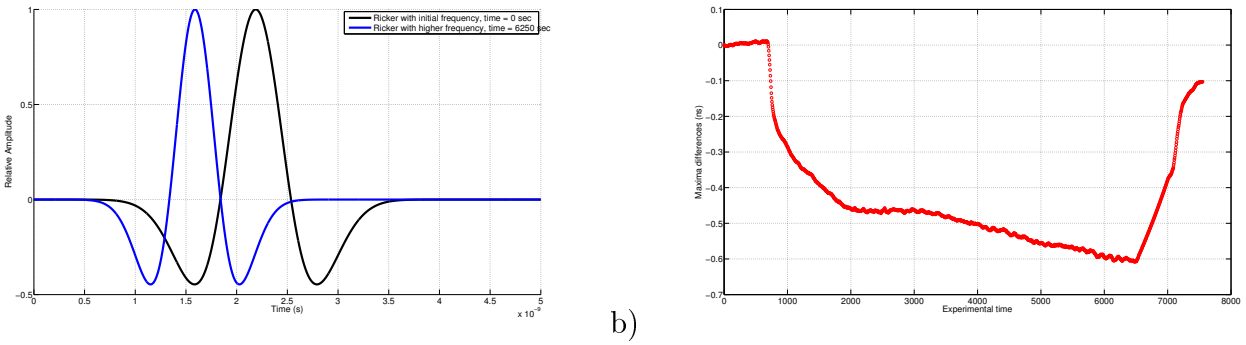

a) b)

Figure 15. a) Time derived Ricker wavelet with two different maximum frequencies, b) computed time delays to be applied to measured TWT of the reflection coming from the bottom of the tank, in the multi-step case.

a)

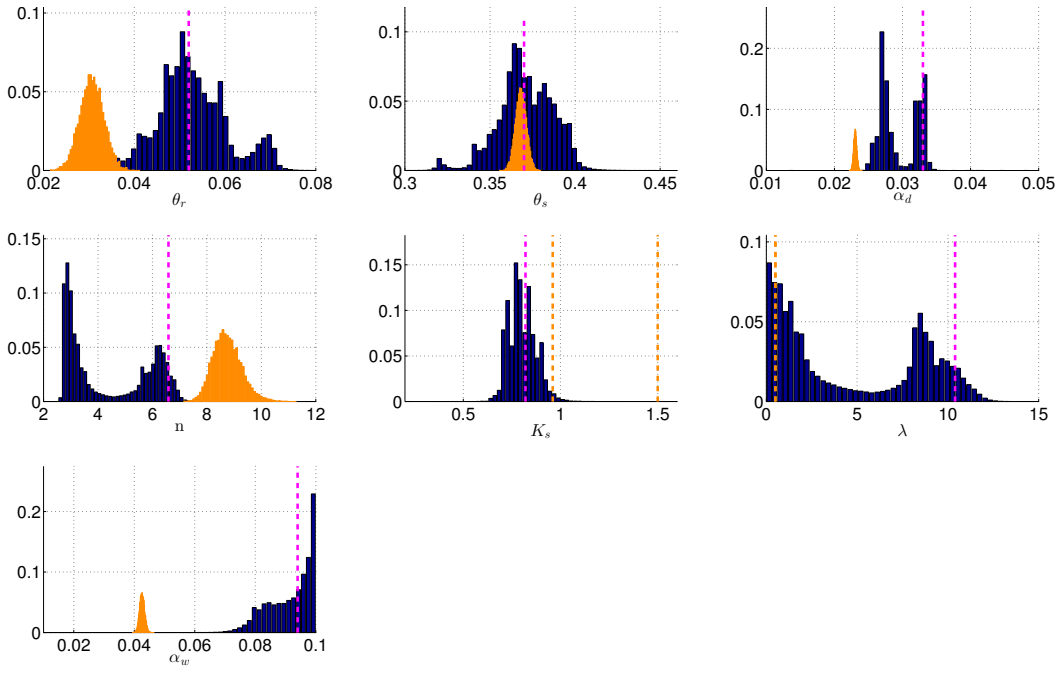

b)

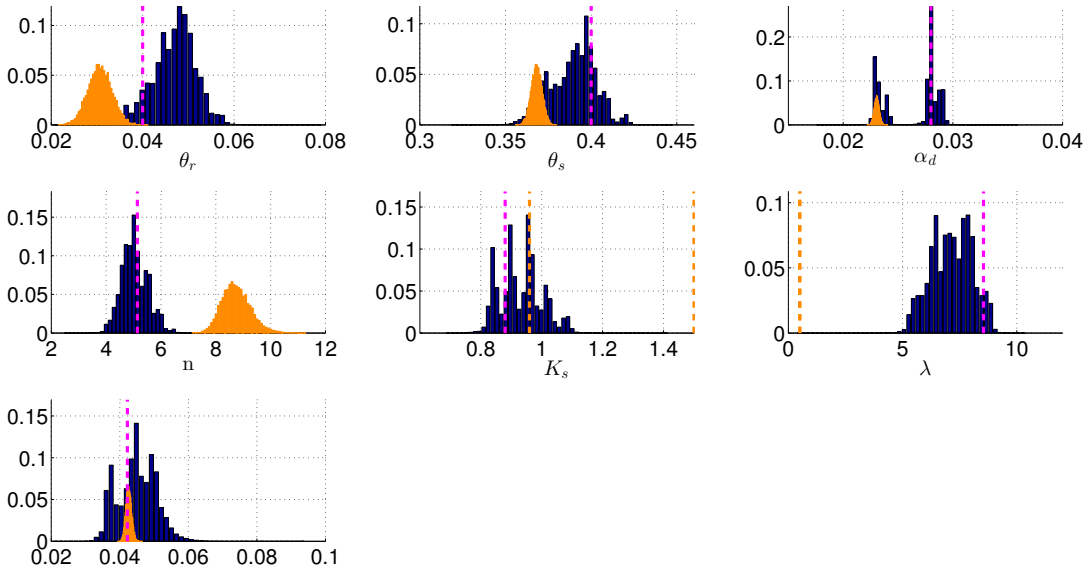

Figure 16. Histograms of the models fitting the experimental a) multi-step data with a RMSE smaller than or equal to 0.154 *ns* and b) one-step data with a RMSE smaller than or equal to 0.163 *ns*. Orange histograms represent the laboratory data obtain with HWC, orange dashed lines limit the range for K_s obtain with KSAT measurement and $\lambda = 0.5$ from *Mualem* [1976]. The pink lines represent the optimized parameters (see Table 2).

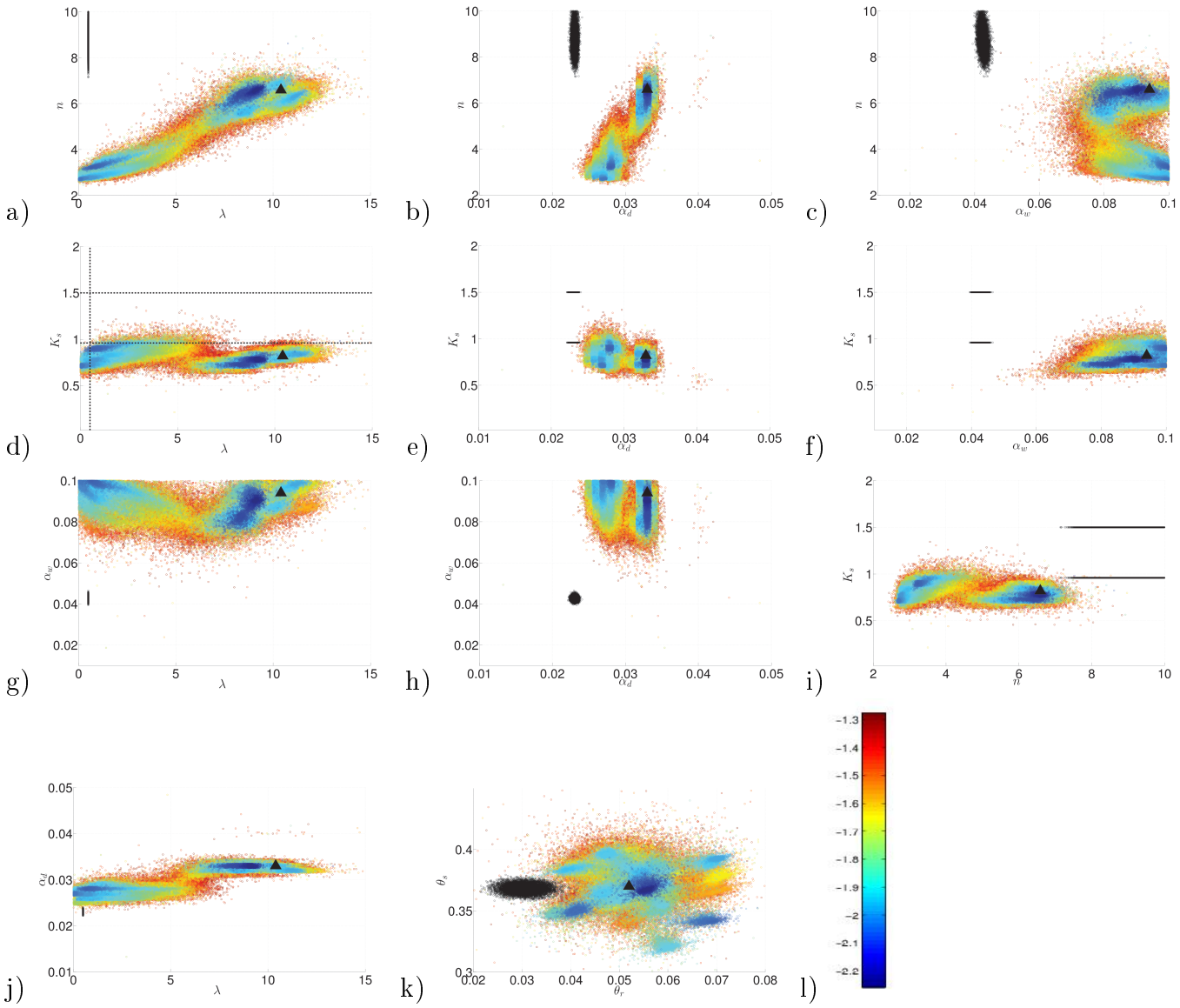

Figure 17. Objective function plots obtained for a multi-step experiment done with 231,192 models fitting experimental data subsets with a RMSE smaller than or equal to $\sigma = 0.154\ ns$. The colorbar corresponds to RMSE values. Black triangles symbolize the parameter set optimizing the original data set sampled with a 20 s time step (giving the best fit with a RMSE of 0.14 ns). The black dots are the parameters estimated from HWC and KSAT experiment, and the usual λ value found in literature.

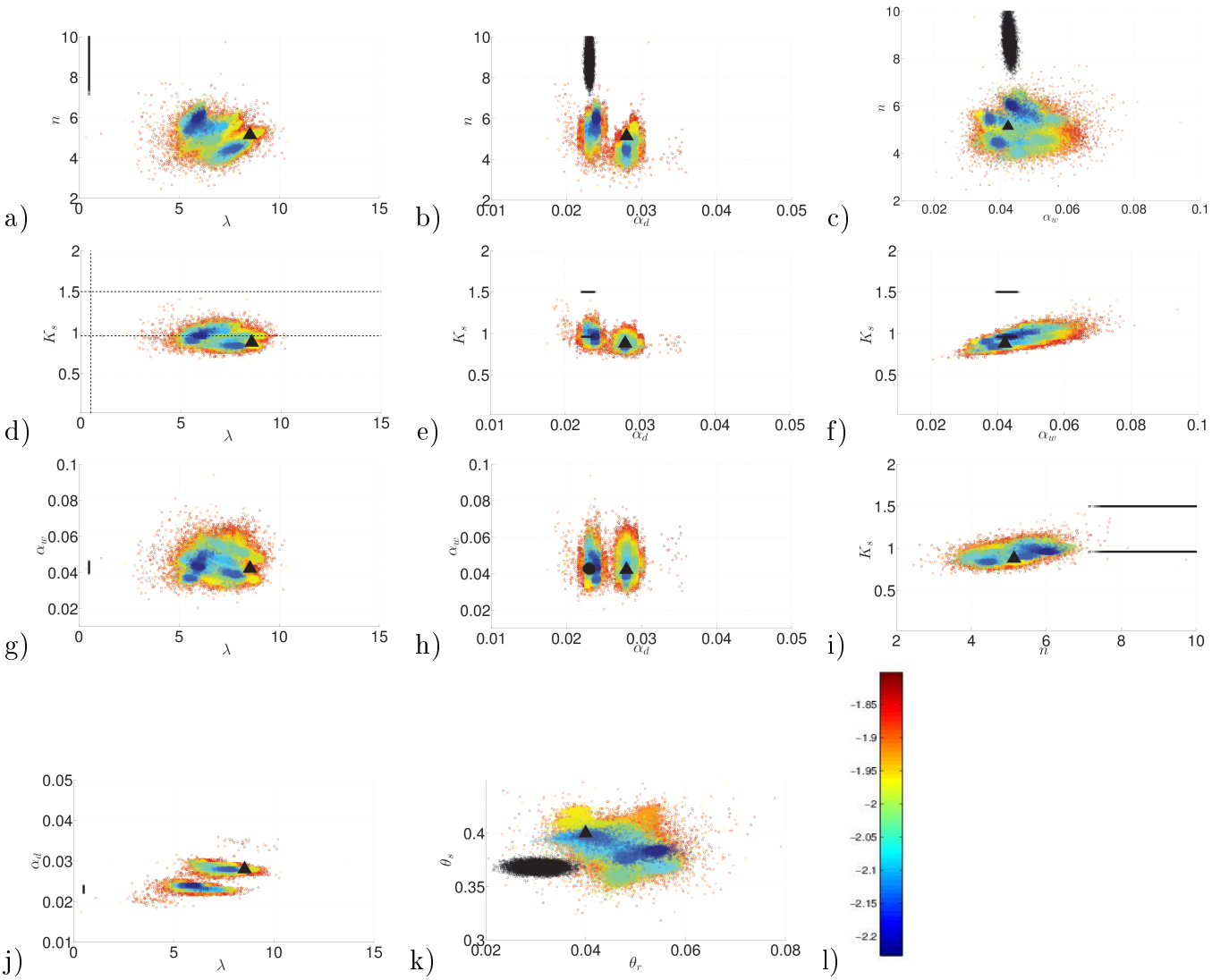

Figure 18. Objective function plots obtained for a one-step experiment done with 238,432 models fitting experimental data subsets with a RMSE smaller than or equal to $\sigma = 0.163\,ns$. The colorbar corresponds to RMSE values. Black triangles symbolize the parameter set optimizing the original data set sampled with a 20 s time step (giving the best fit with a RMSE of 0.148 ns). The black dots are the parameters estimated from HWC and KSAT experiment, and the usual λ value found in literature.